Monthly Notices
of the
ROYAL ASTRONOMICAL SOCIETY

MNRAS **504,** 2405–2419 (2021)
Advance Access publication 2021 March 19

doi:10.1093/mnras/stab635

Particle acceleration and magnetic field amplification in massive young stellar object jets

Anabella T. Araudo [1,2]★ Marco Padovani [3] and Alexandre Marcowith [4]

[1] *ELI Beamlines, Institute of Physics, Czech Academy of Sciences, CZ-25241 Dolní Břežany, Czech Republic*
[2] *Astronomical Institute, Czech Academy of Sciences, Boční II 1401, CZ-141 00 Prague, Czech Republic*
[3] *INAF-Osservatorio Astrofisico di Arcetri, Largo E. Fermi 5, I-50125 Firenze, Italy*
[4] *CNRS/IN2P3, Laboratoire Univers et Particules de Montpellier (LUPM) Université Montpellier, CC72, Place Eugène Bataillon, F-34095 Montpellier Cedex 5, France*

Accepted 2021 February 22. Received 2021 January 26; in original form 2020 June 8

ABSTRACT

Synchrotron radio emission from non-relativistic jets powered by massive protostars has been reported, indicating the presence of relativistic electrons and magnetic fields of strength ∼0.3–5 mG. We study diffusive shock acceleration and magnetic field amplification in protostellar jets with speeds between 300 and 1500 km s^{-1}. We show that the magnetic field in the synchrotron emitter can be amplified by the non-resonant hybrid (Bell) instability excited by the cosmic ray streaming. By combining the synchrotron data with basic theory of Bell instability we estimate the magnetic field in the synchrotron emitter and the maximum energy of protons. Protons can achieve maximum energies in the range 0.04–0.65 TeV and emit γ rays in their interaction with matter fields. We predict detectable levels of γ rays in IRAS 16547−5247 and IRAS 16848−4603. The γ ray flux can be significantly enhanced by the gas mixing due to Rayleigh–Taylor instability. The detection of this radiation by the *Fermi* satellite in the GeV domain and the forthcoming Cherenkov Telescope Array at higher energies may open a new window to study the formation of massive stars, as well as diffusive acceleration and magnetic field amplification in shocks with velocities of about 1000 km s^{-1}.

Key words: acceleration of particles – radiation mechanisms: non-thermal – shock waves – stars: jets – gamma-rays: general.

1 INTRODUCTION

Stars are formed within dense molecular clouds, accreting matter on to the central protostar with the formation of a circumstellar disc and bipolar jets. These ejections are collimated flows of disc/stellar matter accelerated by magnetic field lines (Blandford & Payne 1982; Shu et al. 1994), and moving with speeds $v_j \sim$ 300–1500 km s^{-1} into the ambient molecular cloud. Molecular matter from the cloud is entrained by the jet, forming molecular outflows. Protostellar jets are thermal radio emitters in most of the cases (Anglada, Rodríguez & Carrasco-González 2018). However, radio emission with negative spectral indices has been detected in several protostellar jets suggesting a non-thermal nature of the emission (e.g. Garay et al. 2003; Purser et al. 2016; Rodríguez-Kamenetzky et al. 2017; Obonyo et al. 2019). In the particular case of the jet associated with the massive protostar IRAS 18162−2048 and its famous Herbig–Haro (HH) objects HH 80 and HH 81, Carrasco-González et al. (2010) reported on polarized radio emission and confirmed that the radiation is produced by the synchrotron process. The detection of synchrotron radiation is an evidence that there is a population of mildly relativistic or relativistic electrons in the jet.

The cosmic ray (CR) energy density in molecular clouds is poorly known, but it should be at least of the same order of the CR energy density in the interstellar medium, i.e. $\sim 10^{-12}$ erg cm^{-3} (e.g. Ferrière 2001).[1] Therefore, CRs with energy densities larger than 10^{-8} erg cm^{-3} (see Section 3) have to be locally accelerated at the jet termination shocks or/and in the internal jet shocks. This result is in agreement with Padovani et al. (2015, 2016), who have shown that the large ionization rate estimated from molecular line ratios in L1157-B1 (Podio et al. 2014) and OMC2-FIR4 (Ceccarelli et al. 2014; Fontani et al. 2017; Favre et al. 2018) can be due to local acceleration of thermal particles to a relativistic regime in protostellar jets.

Diffusive shock acceleration (DSA) is the most established mechanism to accelerate particles in sources where shock waves are present, from solar flares (e.g. Chen et al. 2015) to the outskirts of galaxy clusters (e.g. Petrosian 2001). Magnetic turbulence near the shock allows particles to diffuse back and forth the shock front gaining energy at each crossing cycle (Axford, Leer & Skadron 1977; Krymskii 1977; Bell 1978a; Blandford & Ostriker 1978). The maximum energy that particles can achieve in non-relativistic parallel shocks is usually determined by radiative losses or advection escape from the acceleration region. Araudo et al. (2007) showed that completely ionized and fast protostellar jets can accelerate particles up to TeV

[1] Unless a strong source of CRs contributes to a local enhancement, this number is actually an upper limit as CRs are subject to strong ionization losses while propagating in molecular clouds.

★ E-mail: anabella.araudo@eli-beams.eu

energies if Bohm[2] diffusion applies. However, in a non-completely ionized medium, damping of Alfvén (or magnetohydrodynamic) waves by ion-neutral collisions can reduce the particle maximum energy (Drury, Duffy & Kirk 1996; Padovani et al. 2015, 2016).

The detection of molecular emission lines such as Hα, [N II], [S II], and [O III] in HH objects indicates that protostellar jets are not completely ionized. Emission lines are usually associated with internal (low-velocity) shocks in jets emanating from low-mass protostars. However, in sources like HH 80 and HH 81 molecular lines are co-spatial with synchrotron radiation of locally accelerated electrons (Rodríguez-Kamenetzky et al. 2019). Therefore, strong shocks and scattering waves are present in non-completely ionized plasmas. As a result, short-wavelength Alfvén waves are unlikely to scatter particles back and forth the shocks due to their damping by ion-neutral collisions. Bell (2004) realized that under certain conditions non-resonant (hereafter NR) hybrid[3] waves can grow faster than Alfvén (resonant) waves. The NR (Bell) instability has two main advantages: (i) the magnetic field is amplified by orders of magnitude and (ii) NR waves are not strongly damped by ion-neutral collisions, even if the maximum growth rate is reduced (Reville et al. 2007).

In this study, we show that the magnetic field in the synchrotron emitter of high-mass protostellar jets can be amplified by the streaming of CRs (Bell 2004), as in supernova remnants (e.g. Vink & Laming 2003) and jets in active galactic nuclei (Araudo, Bell & Blundell 2015). By assuming that the number of non-thermal electrons and protons is the same, we find that the energy density in non-thermal protons is large enough to drive the Bell instability in the termination region of protostellar jets. In addition, we show that detectable levels of gamma-rays in the GeV domain are expected from protostellar jets. We consider the sample of non-thermal lobes in the termination region of high-mass protostellar jets studied by Purser et al. (2016) with the Australian Telescope Compact Array (ATCA) facility. We select the sources with radio spectral index $0.3 < \alpha < 0.8$, where the radio flux density at frequency ν is $S_\nu \propto \nu^{-\alpha}$. In addition, Obonyo et al. (2019) found that 6 of the 15 massive young stellar objects (MYSOs) observed with the Jansky Very Large Array (JVLA) show clear evidence of non-thermal emission, with spectral indices $\alpha > 0.42$. From this last sample we select the source IRAS 23262+5834. In Table 1, we list the MYSOs selected for our study. They are located at a distance $0.7 \leq d/\mathrm{kpc} \leq 7.8$ from Earth. The jet ionized mass-loss rate is $6 \times 10^{-8} \leq \dot{M}_\mathrm{i}/(\mathrm{M}_\odot\ \mathrm{yr}^{-1}) \leq 5 \times 10^{-5}$ and the kinetic luminosity is $5.3 \times 10^{33} \leq L_\mathrm{kin}/(\mathrm{erg\ s}^{-1}) \leq 4.4 \times 10^{35}$.

The paper is organized as follows: in Section 2, we describe the physical properties of protostellar jets and the condition for them to be non-thermal emitters. In Section 3, the magnetic field and the content of relativistic particles is inferred from synchrotron emission. In Section 4, we discuss both the resonant and non-resonant instabilities in the context of young stellar jets.[4] In Section 5, we briefly describe the non-linear saturation of the amplified magnetic field and determine its strength. In Section 6, we compute the maximum energy of protons and in Section 7 we estimate the γ-ray flux from our source sample. In Section 8, we present our conclusions. Gaussian-cgs units are used throughout the paper.

[2]The Bohm diffusion regime is obtained when the mean-free path of the particle imposed by angular scattering is equal to its Larmor radius.

[3]The term hybrid comes from the nature of the instability which can be described using both magnetohydrodynamic and kinetic theory.

[4]We note that this section is plasma-physics oriented. It is written as a self-contained way. Unfamiliar reader can skip it.

Table 1. Non-thermal MYSOs selected from the observational studies carried out by Purser et al. (2016) and Obonyo et al. (2019). From left to right we list the name of the source in the Green and IRAS catalogues, the distance d, and the ionized mass-loss rate $\dot{M}_\mathrm{i} = X\dot{M}_\mathrm{j}$, where X is the ionization fraction and $\dot{M}_\mathrm{j}$ is the total jet mass-loss rate provided in the literature mentioned before. The values of X and jet velocity fixed by Purser et al. (2016) and Obonyo et al. (2019) to compute $\dot{M}_\mathrm{j}$ are $X = 0.2$ and 0.4, and $v_\mathrm{j} = 500$ km s^{-1}. The jet kinetic luminosity computed as $L_\mathrm{kin} = \dot{M}_i v_\mathrm{j}^2/2$ is also listed.

Source	IRAS name	d [kpc]	$\dot{M}_\mathrm{i}$ [$\mathrm{M}_\odot\ \mathrm{yr}^{-1}$]	X	L_kin [erg s^{-1}]
G263.7434	08470−4321	0.7	6.4×10^{-8}	0.2	3.3×10^{33}
G263.7759	08448−4343	0.7	1.3×10^{-7}	0.2	1.1×10^{34}
G310.1420	13484−6100	5.4	1.1×10^{-6}	0.2	9.2×10^{34}
G313.7654	14212−6131	7.8	4.1×10^{-6}	0.2	3.4×10^{35}
G339.8838	16484−4603	2.7	5.3×10^{-6}	0.2	4.4×10^{35}
G343.1261	16547−4247	2.8	3.5×10^{-6}	0.2	2.9×10^{35}
G114.0835	23262+5834	4.2	4.4×10^{-7}	0.4	3.3×10^{34}

2 PROTOSTELLAR JET PHYSICAL PROPERTIES

The detection of thermal (free–free) and synchrotron emission from protostellar jets indicates that (*i*) there are shocks that heat up the plasma and accelerate particles, (ii) the regions in the jet where thermal and non-thermal emission is radiated are at least partially ionized, and (iii) magnetic fields of about 1–10 mG are needed to explain the detected synchrotron flux if equipartition arguments apply (see Section 3.1). In this section, we provide some constraints on the temperature T_u, the ionization fraction X_u, the ion density n_i, and the magnetic field B_u upstream of the shock of speed v_sh by using the most updated data available in the literature (see Table 2) and conservation equations. We define $X_\mathrm{u} = (n_\mathrm{e} + n_\mathrm{i})/n_\mathrm{j}$, where $n_\mathrm{j} = n_\mathrm{i} + n_\mathrm{e} + n_\mathrm{n}$, n_e and n_n are the free electrons and neutral densities, respectively, and we assume $n_\mathrm{e} = n_\mathrm{i}$ hereafter.

2.1 Ionization fraction and jet temperatures

Bacciotti & Eislöffel (1999) estimated the ionization fraction, X, in a sample of low-mass protostellar jets. They found that X generally decreases almost monotonically along the jet, hence the effects of the shocked materials over X seems to be minor and we may identify X with X_u. Typical values of X_u between 0.02 and 0.4 have been derived by the authors. Maurri et al. (2014) analyzed *Hubble Space Telescope* arc-second images of the DG Tau jet, hence at a much closer location to the central source than Bacciotti & Eislöffel (1999). They found a low-ionization fraction ($\approx$0.02) at the base of the jet, then increasing to a plateau value of $\approx$0.7 at a distance of 3 arcsec from the central source. The ionization fraction seems then to decrease again. By modelling the optical [O II]/[O I] line ratio in shocks at the base of the HN Tau jet, Hartigan, Edwards & Pierson (2004) find $X_\mathrm{u} \approx 0.7$. Teşileanu et al. (2012) developed a magnetohydrodynamic (MHD) model of low-mass protostellar jets and adapted it to the source RW Aur. They found that $X_\mathrm{u} \approx 0.1$–0.2 in the central spine correctly fits the surface brightness fluxes in several forbidden lines. They attributed this ionization fraction to irradiation by X-rays from the protostellar magnetic corona.

The temperature of the unshocked gas is difficult to constrain as line brightness or line ratios are only weakly dependent on it. Garcia et al. (2001) investigated low-mass MHD jets launched from accretion discs including ambipolar diffusion heating and several

Table 2. Observed and derived parameters of non-thermal lobes associated with MYSOs. From left to right we list the name of the source and the non-thermal component in the jet, the observed frequency ν, the measured flux density S_ν, the radio spectral index α, the major ($\theta_{\rm maj}$) and minor axis ($\theta_{\rm min}$) deconvolved dimensions of the component and its average linear size R, the synchrotron emissivity $\epsilon_{\rm synchr}$, the lower limit on the shock velocity $v_{\rm sh,\,ad}$, the density $n_{\dot{M}}$, the upper limit on the lobe density given by equation (6), and the average density $\langle n_i \rangle$. We define $R = (R_{\rm maj} + R_{\rm min})/2$ as the characteristic size of the hotspot, where $R_{\rm min,maj} = 4.8 \times 10^{-6} d\,\theta_{\rm min,maj}$ and d is the source distance given in Table 1.

	Source		ν [GHz]	S_ν [mJy]	α	$\theta_{\rm maj} \times \theta_{\rm min}$ [arcsec^2]	R [cm]	$\epsilon_{\rm synchr}$ [erg cm^{-3}s^{-1}Hz^{-1}]	$v_{\rm sh,\,ad}$ [km s^{-1}]	$n_{\dot{M}}$ [cm^{-3}]	$n_{\rm ff}$ [cm^{-3}]	$\langle n_{\rm i} \rangle$ [cm^{-3}]
(1)	G263.7434	N	9	0.56	0.45	1.23×0.36	4.0×10^{15}	4.7×10^{-30}	317	1.0×10^{3}	1.6×10^{5}	1.2×10^{4}
(2)	G263.7759	NW	17	2.16	0.78	1.64×0.34	5.0×10^{15}	9.4×10^{-30}	353	1.3×10^{3}	2.2×10^{5}	1.7×10^{4}
(3)	G310.1420	A4	9	0.93	0.70	1.10×0.89	3.3×10^{16}	8.4×10^{-31}	373	2.5×10^{2}	6.6×10^{4}	4.1×10^{4}
(4)		D	9	1.93	0.46	1.38×1.05	4.8×10^{16}	1.2×10^{-30}	377	2.7×10^{2}	8.0×10^{5}	4.7×10^{4}
(5)	G313.7654	A2	9	0.14	0.68	0.85×0.38	6.6×10^{16}	2.3×10^{-31}	495	8.6×10^{2}	3.4×10^{4}	5.4×10^{3}
(6)		D	5.5	0.15	0.32	0.80×0.41	3.4×10^{16}	2.6×10^{-31}	497	8.9×10^{2}	3.5×10^{4}	5.6×10^{3}
(7)	G339.8838	NE	9	2.36	0.39	0.47×0.38	8.1×10^{15}	1.3×10^{-28}	842	7.9×10^{4}	8.5×10^{5}	2.6×10^{5}
(8)		SW	9	1.50	0.72	5.33×0.85	6.5×10^{16}	5.6×10^{-32}	463	3.7×10^{2}	1.7×10^{4}	2.5×10^{3}
(9)	G343.1261*	N4	17	1.80	0.67	0.65×0.35	1.0×10^{16}	3.2×10^{-29}	674	1.6×10^{4}	4.2×10^{5}	8.2×10^{4}
(10)		S1	17	4.72	0.45	0.64×0.35	1.0×10^{16}	3.8×10^{-29}	633	9.2×10^{3}	4.6×10^{5}	6.5×10^{4}
(11)	G114.0835	B	1.5	0.21	0.42	2.50×1.20	1.1×10^{17}	2.3×10^{-32}	271	0.3×10^{2}	1.0×10^{4}	6.1×10^{2}
	Average values				0.55	1.46×0.57	3.3×10^{16}	1.8×10^{-30}	455	1.2×10^{3}	1.0×10^{5}	1.6×10^{4}
						Observational data				Section 2.2		

sources of ionization (X-rays and UV radiation as well as collisions). They found a typical jet temperature $T_{\rm u} \approx 10^4$ K.

In high-mass protostars both $X_{\rm u}$ and $T_{\rm u}$ are barely known or even constrained. Following Garcia et al. (2001) we can reasonably expect the jets from high-mass protostars to have higher mass-loss rates and to be denser and cooler than jets from low-mass protostars. Values of $X_{\rm u}$ as small as 10^{-4} are found for jets with $T_{\rm u} \approx 10^4$ K. However, other sources of heating like turbulence, MHD wave dissipation, magnetic reconnection, or weak shock heating have not been considered in this work. In a very recent study, Fedriani et al. (2019) found that the ionization fraction in the jet of the high-mass protostar G35.20−0.74N is ∼0.1, similar to the values for low-mass protostars. Purser et al. (2016) assumed $X_{\rm u} = 0.2$ for jets powered by high-mass protostars. For our study we select $0.1 \leq X_{\rm u} \leq 1$ and $T_{\rm u} = 10^4$ K in MYSO jets. Hotter (colder) jets likely have higher (lower) ionization fraction.

2.2 Shocks and densities

Internal shocks due to a variable ejection velocity is the most popular model to explain the chain of knots in protostellar jets such as HH 111 (Raga et al. 1990). In most of the cases, knots are bright Hα and [S II] emitters in the optical band indicating shock speeds of few tens of km s^{-1}, much smaller than typical proper motions with speeds of hundreds km s^{-1}. Since velocity perturbations are of the order of 10 per cent of the jet speed, $v_{\rm j}$ (Reipurth & Bally 2001), internal shocks are not fast enough to accelerate particles up to very high energies, which is consistent with the fact that most of the knots (and HH objects) are thermal emitters (however, see Osorio et al. 2017; Rodríguez-Kamenetzky et al. 2017, for some exceptions).

Non-thermal emission has been detected in the outer lobes of a handful of protostellar jets, which is more consistent with the presence of a strong adiabatic shock at the location of the non-thermal emitter where synchrotron-emitting electrons are accelerated. In the jet termination region, where the jet impacts against the external medium (see Fig. 1), the bow shock moves into the molecular cloud at a speed $v_{\rm bs} \sim v_{\rm j}/(1 + 1/\beta\sqrt{\chi})$, where $\chi \equiv n_{\rm j}/n_{\rm mc}$ is the jet ($n_{\rm j}$) to molecular cloud ($n_{\rm mc}$) density contrast, and $\beta \equiv R_{\rm h}/R_{\rm j}$, being $R_{\rm j}$ and $R_{\rm h}$ the radius of the jet beam and head, respectively (e.g. Hartigan 1989; Chernin et al. 1994; Raga, Canto & Cabrit 1998). The reverse shock (or Mach disc) in the jet moves at $v_{\rm rs} = v_{\rm j} - 3v_{\rm bs}/4$. In 'heavy' jets ($\chi > 1$), the bow shock is faster than the Mach disc,[5] whereas in 'light' jets ($\chi < 1$), the reverse shock is faster than the bow shock. In particular, $v_{\rm rs} \sim v_{\rm j}$ and $v_{\rm bs} \sim v_{\rm j}\sqrt{\chi}$ when $\chi \ll 1$, whereas $v_{\rm bs} \sim v_{\rm j}$ when $\chi \gg 1$. As an example, $v_{\rm rs}$ and $v_{\rm bs}$ are ∼750 and 250 km s^{-1}, respectively, when $v_{\rm j} = 1000$ km s^{-1} and $\chi = 0.1$. Proper motions of about 300–1400 km s^{-1} have been observed in protostellar jets (e.g. Marti, Rodriguez & Reipurth 1993; Masqué et al. 2012), and therefore we can expect jet velocities comparable to or larger than these values.

The detection of GeV photons from classical novae (Ackermann et al. 2014) indicates that radiative shocks with velocities ≤1000 km s^{-1} can accelerate particles up to ∼10 GeV (see e.g. Vurm & Metzger 2018). This study concentrates, however, on adiabatic (i.e. non-radiative) shocks. The condition for a shock with velocity $v_{\rm sh}$ to be adiabatic is $q \equiv l_{\rm th}/R_{\rm j} > 1$ (Blondin, Fryxell & Konigl 1990), where we define $R_{\rm j}$ as the radius of the section of the jet at the position of the hotspot. The thermal cooling length is

$$\frac{l_{\rm th}}{\rm cm} \simeq 6.9 \times 10^{16} \left(\frac{n_{\rm u}}{10^4\ {\rm cm^{-3}}}\right)^{-1} \left(\frac{v_{\rm sh}}{1000\ {\rm km\ s^{-1}}}\right)^{\frac{9}{2}} \quad (1)$$

(e.g. Raga, Noriega-Crespo & Velázquez 2002), where $n_{\rm u}$ is the density upstream of the shock. The condition $q > 1$ can be rewritten as $v_{\rm sh} > v_{\rm sh,\,ad}$, where

$$\frac{v_{\rm sh,ad}}{\rm km\ s^{-1}} \simeq 650 \left(\frac{n_{\rm u}}{10^4\ {\rm cm^{-3}}}\right)^{\frac{2}{9}} \left(\frac{R_{\rm j}}{10^{16}\ {\rm cm}}\right)^{\frac{2}{9}}. \quad (2)$$

The reverse-shock to bow-shock cooling parameter ratio is $q_{\rm rs}/q_{\rm bs} = l_{\rm rs}/l_{\rm bs} \sim \chi^{-3.25}$ indicating that the termination region of light jets ($\chi < 1$) is composed by an adiabatic Mach disc and a radiative bow shock.

The jet ion density can be estimated as

$$\frac{n_{\dot{M}}}{\rm cm^{-3}} \approx 150 \left(\frac{\dot{M}_{\rm i}}{10^{-6}\ {\rm M_\odot\ yr^{-1}}}\right) \left(\frac{v_{\rm j}}{1000\ {\rm km\ s^{-1}}}\right)^{-1} \left(\frac{R_{\rm j}}{10^{16}\ {\rm cm}}\right)^{-2} \quad (3)$$

[5]This situation is very similar to the cloudlet model (Norman & Silk 1979) where a fast cloud moves into a molecular cloud (see e.g. Hartigan 1989) or into a slow jet (Yirak et al. 2012).

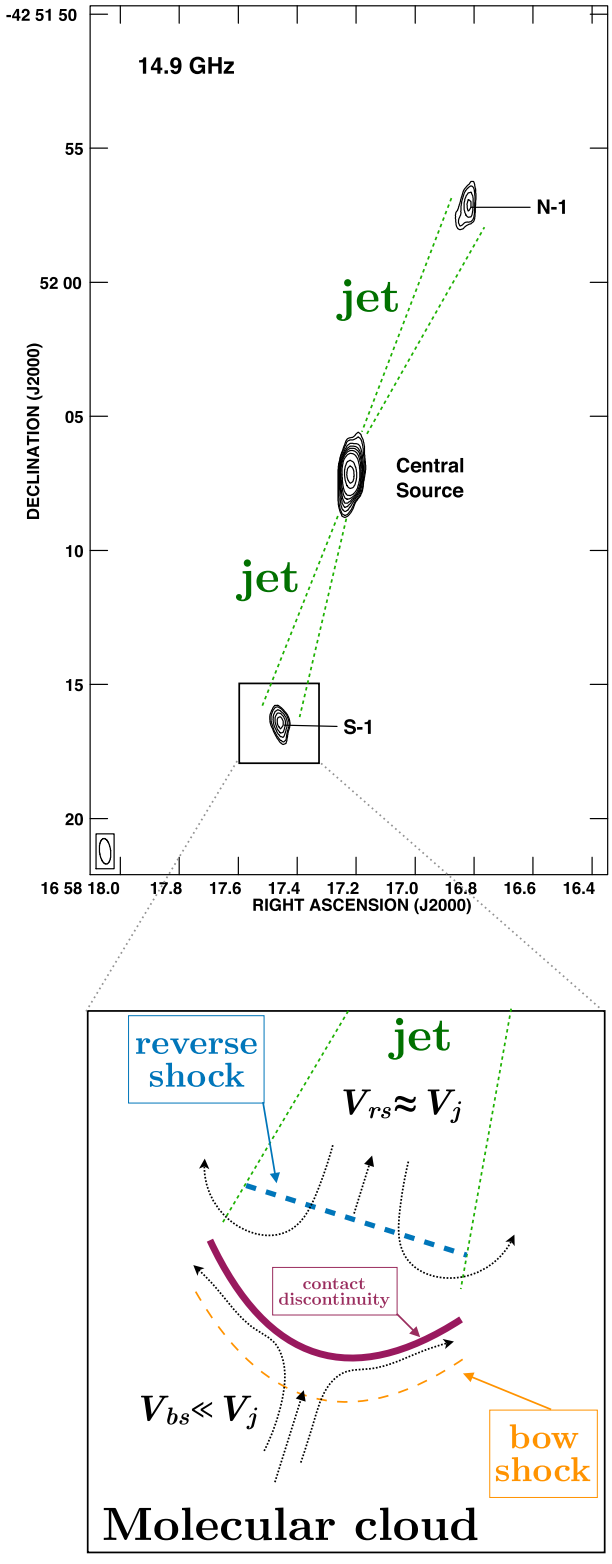

Figure 1. Top: The radio image of the source IRAS 16547−4247 (G343.1261) at 14.9 GHz (adapted from Rodríguez et al. 2005). Bottom: Sketch of the jet termination region in light protostellar jets. Here, $V_{\rm bs}$, $V_{\rm rs}$, and $V_{\rm j}$ refer to the bow shock, the reverse shock, and the jet velocity, respectively.

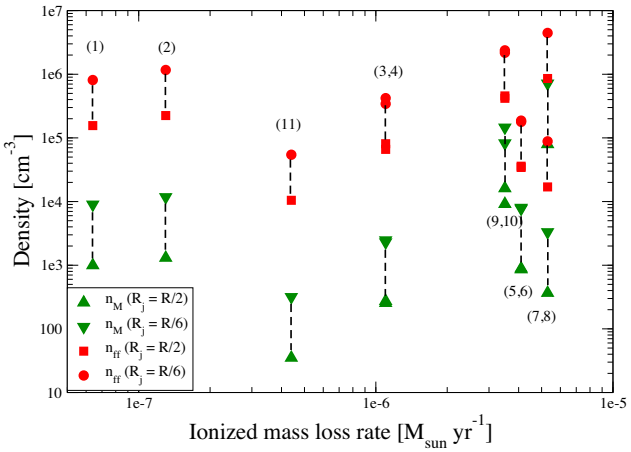

Figure 2. Jet ion density, $n_{\dot{M}}$, for the sources listed in Table 2 as a function of the ionized mass-loss rate assuming $R_{\rm j} = R/2$ (green triangles up) and $R/6$ (green triangles down). The red squares and circles indicate the value of $n_{\rm ff}$ when $R_{\rm j} = R/2$ and $R/6$, respectively.

(e.g. Rodríguez-Kamenetzky et al. 2017). Owing to the large uncertainties in the different parameters we neglect the contribution of helium in equation (3). In Fig. 2, we plot $n_{\dot{M}}$ for $R_{\rm j} = R/2$ and $R/6$, where R is the average linear size of the hotspot also listed in Table 2. The jet mass-loss rate of ionized matter $\dot{M}_{\rm i} \propto v_{\rm j}$ is assumed to be constant along the jet and then $n_{\dot{M}}$ turns out to be independent of the jet velocity. By inserting equation (3) in equation (2) we find that $v_{\rm sh,ad} \propto R_{\rm j}^{-2/9}$. In Table 2, we list $n_{\dot{M}}$ and $v_{\rm sh,\,ad}$ assuming $R_{\rm j} = R/2$. We note that $n_{\dot{M}}$ is a rough estimation of the jet ion density given the uncertainties in the values of $\dot{M}_{\rm i}$ and $R_{\rm j}$. In particular, light adiabatic jets form a cocoon and therefore the size of the non-thermal lobe at the jet head is expected to be $R_{\rm h} > R_{\rm j}$. Krause (2003) found that $(R_{\rm j}/R_{\rm h})^2 \sim 0.1$–1 when $\chi > 0.01$; this gives an increment in the jet density by a factor of ∼10 when $R_{\rm j} = R/6$ instead of $R/2$ (see Fig. 2). Nevertheless, the derived jet density is likely lower than the typical density values of $\sim 10^5$ cm^{-3} in the molecular clouds where massive stars form (Hennebelle & Falgarone 2012) giving $\chi < 1$. Therefore, $q_{\rm rs} > q_{\rm bs}$ and we should rather expect non-thermal sources in light jets ($\chi < 1$), where the reverse shock is faster than the bow shock.

In order to check if synchrotron emission comes from the reverse-shock rather than from the bow-shock downstream region, we compare the synchrotron ($\epsilon_{\rm synchr,\,\nu}$) and free–free ($\epsilon_{\rm ff,\,\nu}$) emissivities. The temperature of the plasma immediately downstream of the shock with compression ratio $r = 4$ is $T_{\rm d} \sim 2.3 \times 10^7\ (v_{\rm sh}/1000\,{\rm km\,s^{-1}})^2$ K. The free–free emissivity of the shocked plasma emitted at frequency $\nu \ll k_{\rm B} T_{\rm d}/h \sim 480 (v_{\rm sh}/1000\,{\rm km\,s^{-1}})^2$ GHz is

$$\frac{\epsilon_{\rm ff,\nu}}{\rm erg\,cm^{-3}s^{-1}Hz^{-1}} \approx 1.4 \times 10^{-33} g(\nu, T_{\rm d}) \times \left(\frac{n_{\rm e}}{10^4\ {\rm cm^{-3}}}\right)^2 \left(\frac{v_{\rm sh}}{1000\ {\rm km\,s^{-1}}}\right)^{-1} \quad (4)$$

(Lang 1974), where $k_{\rm B}$ and h are the Boltzmann and Planck constants, respectively. The Gaunt factor is $g(\nu, T_{\rm d}) \sim 0.54 \log \Lambda$ and

$$\Lambda \approx 1.1 \times 10^9 \left(\frac{v_{\rm sh}}{1000\,{\rm km\,s^{-1}}}\right)^2 \left(\frac{\nu}{\rm GHz}\right)^{-1} \quad (5)$$

when $2\pi\nu \gg \omega_{\rm p}$ and $T_{\rm d} > 3.6 \times 10^5$ K. Here, $\omega_{\rm p} \sim 5.6 \times 10^6 \sqrt{n_{\rm e}/10^4\,{\rm cm^{-3}}}$ rad s^{-1} is the electron plasma frequency. We note that $g(\nu, T) \sim 4.3$ when $v_{\rm sh} = 1000$ km s^{-1} and $\nu \sim 10$ GHz.

On the other hand, the synchrotron emissivity of a source located at distance d is $\epsilon_{\rm synchr,\,\nu} = 4\pi d^2 S_\nu / V_{\rm e}$, where S_ν is the synchrotron

flux measured at frequency ν and $V_e \sim R_j^3$ is the volume of the synchrotron emitter (see equation A1). By imposing $\epsilon_{\mathrm{synchr},\,\nu} > \epsilon_{\mathrm{ff},\,\nu}$, we find that the density of thermal electrons downstream of the shock has to be smaller than n_{ff}, where

$$\frac{n_{\mathrm{ff}}}{\mathrm{cm^{-3}}} \approx 1.4 \times 10^5 \left(\frac{d}{\mathrm{kpc}}\right) \left(\frac{S_\nu}{\mathrm{mJy}}\right)^{\frac{1}{2}} \left(\frac{R_j}{10^{16}\,\mathrm{cm}}\right)^{-\frac{3}{2}} \left(\frac{v_{\mathrm{sh}}}{1000\,\mathrm{km\,s^{-1}}}\right)^{\frac{1}{2}} \quad (6)$$

for the non-thermal emission to dominate at frequency ν (see Henriksen, Mirabel & Ptuskin 1991). In Fig. 2, we plot n_{ff} and in Table 2 we list the values of n_{ff} for the case $v_{\mathrm{sh}} = 1000$ km s^{-1} and $R_j = R/2$. We can see that molecular clouds with densities $\sim 10^5$ cm^{-3} will not (or marginally) satisfy the condition $n_{\mathrm{mc}} < n_{\mathrm{ff}}$ for hosting the synchrotron emitter in the shocked region downstream of the bow shock. On the other hand, $n_{\dot{M}} \ll n_{\mathrm{ff}}$ for all the sources in the sample.

Hereafter, we will consider light jets ($\chi < 1$) for which the synchrotron radiation dominates over the free–free emission and identify the reverse shock with jet speed ($v_j = v_{\mathrm{rs}}$). In order to simplify the notation we will name it v_{sh} and use 1000 km s^{-1} as a characteristic value.[6] The jet ion density will be $n_{\dot{M}} \leq n_i \leq n_{\mathrm{ff}}$ with a mean value $\langle n_i \rangle = \sqrt{n_{\dot{M}} n_{\mathrm{ff}}}$ (see Table 2). We note that $\langle n_i \rangle$ is similar to $n_{\dot{M}}$ when $R_j = R/6$. In Fig. 1, we show a sketch of the scenario considered in this study.

Setting constraints on n_i and v_{sh} is highly important in our study given that the jet kinetic energy density

$$\frac{U_{\mathrm{kin}}}{\mathrm{erg\,cm^{-3}}} \simeq \frac{1.7 \times 10^{-4}}{X_u} \left(\frac{n_i}{10^4\,\mathrm{cm^{-3}}}\right) \left(\frac{v_{\mathrm{sh}}}{1000\,\mathrm{km\,s^{-1}}}\right)^2, \quad (7)$$

and the jet kinetic luminosity

$$\frac{L_{\mathrm{kin}}}{\mathrm{erg\,s^{-1}}} \simeq \frac{2.1 \times 10^{37}}{X_u} \left(\frac{n_i}{10^4\,\mathrm{cm^{-3}}}\right) \left(\frac{v_{\mathrm{sh}}}{1000\,\mathrm{km\,s^{-1}}}\right)^3 \left(\frac{R_j}{10^{16}\,\mathrm{cm}}\right)^2 \quad (8)$$

represent the energy budget to accelerate particles at the shock. Another very important parameter in our study is the magnetic field.

2.3 Magnetic fields

Maser emission provides information about the orientation and strength of magnetic fields in the molecular outflows associated with the central jet. Goddi et al. (2017) derived magnetic field strengths between 100 and 300 mG in the protostellar jet W3(H_2O), which likely results from strong gas compression behind shocks associated with the outflow expansion in the ambient molecular cloud. However, it is difficult to infer the magnetic field orientation and strength in the central jet itself where the origin of the magnetic field is more likely connected to the ejection process from the accretion disc. Lee et al. (2018) reported on the detection of SiO line polarization in the HH 211 protostellar jet, with an estimated magnetic field of about 15 mG at $\sim$300 au from the central protostar.

Theoretical studies of magnetically accelerated jets require the action of a poloidal component to accelerate the plasma and a toroidal component to confine it (Casse & Keppens 2002). The toroidal component evolves with the distance z from the star along the jet as $B_\phi \propto 1/z$. At the jet base, on the edge of the disc, typical values of the magnetic field strength are obtained from the local beta plasma parameter $\beta_p = P_g/P_m$, where P_g and P_m are the gas and magnetic pressures, respectively. Jet launching requires $\beta_p \geq 1$ (Casse & Keppens 2002) giving an upper limit for the magnetic field strength at the base of the jet of $0.3(n_{\mathrm{disc}}/10^{10}\,\mathrm{cm^{-3}})(T_{\mathrm{disc}}/10^3\,\mathrm{K})$ G, where n_{disc} and T_{disc} are the gas density and temperature in the disc, respectively.

Using the model of Combet & Ferreira (2008) we can infer typical values of the vertical magnetic field strength in jet-emitting discs $B_z \sim 0.1$–10 G at 1 au from the star depending on the central mass of the object and the accretion rate. We will henceforth consider typical magnetic field strengths at the base of the jet in the range 10 mG–10 G to be conservative. By using a $1/z$ dilution factor, we obtain typical magnetic field strengths of $B_j \sim 10$ μG–10 mG at distances of the jet termination shock of $\sim 10^3$ au or 10 times smaller at a distance of 10^4 au. By considering the flux-freezing condition, Hartigan et al. (2007) showed that the magnetic field strength of variable MHD jets can be described by the relation $(B_j/15\,\mu\mathrm{G}) \sim (n_i/100\,\mathrm{cm^{-3}})^{0.85}$ giving values in agreement with the above estimate. However, at distances larger than $\sim 10^3$ au from the protostar, densities and magnetic fields are mostly influenced by shocks and rarefaction waves.

The magnetic field topology at the jet termination shock in high-mass protostars is difficult to assess, but it is likely helical due to a combination of a toroidal and a poloidal component (Cerqueira, de Gouveia dal Pino & Herant 1997; Cécere et al. 2016), hence the orientation of the magnetic field with respect to the normal of the termination shock front is likely oblique. On the other hand, numerical studies of non-relativistic and magnetically driven jets show that kink instabilities destroy the ordered helical structure of the magnetic field. Moll (2009) showed that at $z \gtrsim 2$–$15 R_A$, the toroidal field is dissipated and the poloidal component dominates. Here, R_A is the Alfvén radius, where the poloidal jet and the Alfvén speeds are equal. For the objects of interest, this length-scale is typically less than a few tens of au (Pelletier & Pudritz 1992). A dominant poloidal field is also supported by laboratory experiments (Albertazzi et al. 2014).

In this work, acknowledging for the above uncertainties, we adopt $B_j = 10\,\mu$G as a characteristic value of the jet magnetic field in the termination region. The Alfvén speed in the jet is given by

$$\frac{v_A}{\mathrm{km\,s^{-1}}} \simeq 0.2 \left(\frac{B_j}{10\,\mu\mathrm{G}}\right) \left(\frac{n_i}{10^4\,\mathrm{cm^{-3}}}\right)^{-\frac{1}{2}}, \quad (9)$$

and the Alfvén Mach number is

$$M_A = \frac{v_{\mathrm{sh}}}{v_A} \simeq 4800 \left(\frac{v_{\mathrm{sh}}}{1000\,\mathrm{km\,s^{-1}}}\right) \left(\frac{B_j}{10\,\mu\mathrm{G}}\right)^{-1} \left(\frac{n_i}{10^4\,\mathrm{cm^{-3}}}\right)^{\frac{1}{2}}. \quad (10)$$

To keep the calculations simple, we derive most of estimates in the parallel shock configuration (i.e. with a purely poloidal magnetic field), but we discuss in Section 4.1 the impact of the magnetic field obliquity on our results.

3 RELATIVISTIC PARTICLES AND SYNCHROTRON RADIATION

The energy distribution of particles downstream of a shock is a Maxwellian (thermal) distribution with a power-law (non-thermal) tail at a high energies. The transition energy between both distributions is unknown. By using hybrid simulations of parallel non-relativistic shocks, Caprioli & Spitkovsky (2014a) have shown that immediately behind the shock there is a *bridge* of suprathermal ions smoothly connecting the thermal peak with the power-law, while far downstream there is a sharp boundary between thermal and non-thermal protons at $E_{\mathrm{inj,\,p}} \sim 4E_{\mathrm{th}}$, where $E_{\mathrm{th}} = m_p v_{\mathrm{sh}}^2/2 \sim 5.2(v_{\mathrm{sh}}/1000\,\mathrm{km\,s^{-1}})^2$ keV, in agreement with Bell (1978b). Park,

[6] This value probably overestimates the effective v_{rs} but, on the other hand, v_j deduced from proper motions is underestimated given that it corresponds to the velocity projected on the plane of the sky.

Caprioli & Spitkovsky (2015) have shown that the typical energy needed for electron injection into the shock acceleration is comparable with $E_{\rm inj,\,p}$. Achieving such injection energy $E_{\rm inj}$ is much more difficult for electrons, as their initial momentum is a factor $m_{\rm p}/m_{\rm e}$ smaller. In dense and non-completely ionized medium, ionization and Coulomb losses can suppress the acceleration of low-energy particles. Ionization and Coulomb losses are almost constant at energies below $E_0 = 10^{-4} m_{\rm p}c^2$ and $E_{\rm th} = 4\times10^{-6}(T/10^4{\rm K}){\rm m_p c^2}$, respectively, and therefore they cannot quench the acceleration at the injection energy if

$$\frac{n_{\rm i}}{\rm cm^{-3}} < \frac{2.5\times10^7}{\kappa}\left(\frac{B_{\rm j}}{10\,\mu{\rm G}}\right)\left(\frac{v_{\rm sh}}{1000\,{\rm km\,s^{-1}}}\right)^2\frac{1}{\mathcal{F}}, \tag{11}$$

where $\kappa \geq 1$ indicates the departure from the Bohm diffusion regime, $\mathcal{F} = \max[X_{\rm u}/\sqrt{T_{\rm u,4}}, (1-X_{\rm u})]$, and $T_{\rm u,\,4} = T_{\rm u}/10^4$ K (Drury et al. 1996). For typical parameters in jets from high-mass protostars, and $X_{\rm u} > 0.1$ neither ionization nor Coulomb losses quench the acceleration at any energy. We consider that the spectrum of accelerated particles is given by equation (B1).

3.1 Non-thermal electrons

Synchrotron emission at frequency ν in a magnetic field $B_{\rm s}$ is mostly produced by electrons with energy

$$\frac{E_{\rm e}}{\rm MeV} \simeq 475\left(\frac{\nu}{\rm GHz}\right)^{1/2}\left(\frac{B_{\rm s}}{\rm mG}\right)^{-1/2}, \tag{12}$$

indicating that synchrotron photons in the range 100 MHz–10 GHz correspond to relativistic electrons with energies in the range 150 MeV–1.5 GeV, when $B_{\rm s} = 1$ mG. The energy density in non-thermal electrons following a power-law distribution $N_{\rm e} = K_{\rm e}E_{\rm e}^{-s}$ is $U_{\rm e,\,tot} = K_{\rm e}f_{\rm e}$, where $f_{\rm e}$ is defined in equation (B2) and $s = 2\alpha + 1$. For this study we select non-thermal lobes with $0.3 < \alpha < 0.8$ and then $1.6 < s < 2.6$. The normalization factor $K_{\rm e}$ can be determined from the measured synchrotron flux S_ν at a particular frequency ν, as described in Appendix A. By combining equations (A5) and (B4) we find that

$$\frac{U_{\rm e,tot}}{\rm erg\,cm^{-3}} \approx 4.8\times10^{-8}\xi_K(s)\left(\frac{f_e}{10}\right)\left(\frac{\nu}{\rm GHz}\right)^{\frac{s-1}{2}}\times \left(\frac{\epsilon_{{\rm syn},\nu}}{10^{-30}\,{\rm erg\,s^{-1}\,cm^{-3}Hz^{-1}}}\right)\left(\frac{B_{\rm s}}{\rm mG}\right)^{-\frac{(s+1)}{2}}, \tag{13}$$

where $\xi_K(s)$ is given in equation (A6) and $B_{\rm s}$ is the magnetic field in the synchrotron emitter, i.e. mostly coming from the shock downstream medium.[7] The magnitude of $B_{\rm s}$ is unknown. It is commonly assumed that B_s is in equipartition with non-thermal particles, satisfying the minimum energy requirement to explain the synchrotron emission. By setting $U_{\rm e,tot} = B_{\rm s}^2/(8\pi)$ we find that the magnetic field in equipartition with relativistic electrons is

$$\frac{B_{\rm eq,e}}{\rm mG} \approx \xi_{\rm eq}(s)\left(\frac{f_{\rm e}}{10}\right)^{\frac{2}{s+5}}\times \left(\frac{\epsilon_{{\rm syn},\nu}}{10^{-30}\,{\rm erg\,s^{-1}\,cm^{-3}\,Hz^{-1}}}\right)^{\frac{2}{s+5}}\left(\frac{\nu}{\rm GHz}\right)^{\frac{s-1}{s+5}}, \tag{14}$$

where $\xi_{\rm eq}(s) \simeq (1.2\xi_{\rm K}(s))^{2/(s+5)}$ is plotted in Fig. A1.

[7] Depending of the properties of the turbulence around the shock, the magnetic field strength in the synchrotron-emitting region has to account for the residence times of the particles downstream and upstream. The exact expression is given by equation (18) in Parizot et al. (2006).

3.2 Non-thermal protons

The energy density in protons with energy $E_{\rm p} \geq m_{\rm i}c^2$ is $U_{\rm p,tot} = aU_{\rm e,tot}$, where $a = (m_{\rm p}/m_{\rm e})^{(s-1)/2}f_{\rm p}/f_{\rm e}$ (see Appendix B). The non-thermal energy density is $U_{\rm nt} = U_{\rm p,\,tot} + U_{\rm e,\,tot} = (1+a)U_{\rm e,\,tot}$, and then the magnetic field in equipartition with non-thermal electrons and protons is

$$B_{\rm eq} = (1+a)^{\frac{1}{2}}B_{\rm eq,e}. \tag{15}$$

In Table 3, we list the values of s, a, and $B_{\rm eq}$ for all the sources in Table 2 and considering $E_{\rm e,max} = 0.1$ TeV in $f_{\rm e}$. However, we note that $B_{\rm eq} \propto f_{\rm e}^{2/(s+5)}$ and therefore the dependence on $E_{\rm e,max}$ is negligible. We also point out that $B_{\rm eq}$ is an upper limit for the magnetic field in the synchrotron emitter. In Fig. 3, we plot $U_{e,\rm tot}$ for $B_{\rm s} \leq B_{\rm eq}$. The orange and violet circles correspond to the case where the total acceleration efficiency in non-thermal electrons and protons is $U_{\rm nt}/U_{\rm kin} = 1$ and we fixed $v_{\rm sh} = 1000$ km s^{-1} and $n_i = \langle n_{\rm i}\rangle$ and n_M, respectively, to compute $U_{\rm kin}$.

We define the total proton acceleration efficiency $\eta_{\rm p,\,tot} = U_{\rm p,\,tot}/U_{\rm kin}$. These protons can excite various types of instabilities at different scales (see e.g. Marcowith et al. 2016, for a review). In particular they drive a current that combined with small perturbations present in the magnetic field can excite NR waves (Bell 2004). Previous studies of DSA in protostellar jets consider that particles diffuse back and forth the shock due to (resonant) Alfvén waves (e.g. Crusius-Watzel 1990; Henriksen et al. 1991; Araudo et al. 2007; Bosch-Ramon et al. 2010; Padovani et al. 2015). However, we will see that, if the jet (unperturbed) magnetic field $B_{\rm j}$ is smaller than a certain value and the driving parameter (related to the CR current in the upstream medium) $\zeta = 2\eta_{\rm p}v_{\rm sh}/c$ is high enough, the dominant instability is non-resonant. The acceleration efficiency $\eta_{\rm p}$ of protons with particular energy $E_{\rm p}$ and energy density $U_{\rm p}$ in equation (B4) is defined as $\eta_{\rm p} = U_{\rm p}/U_{\rm kin} = \eta_{\rm p,tot}E_p^{-p+2}/f_{\rm p}$, where $f_{\rm p}$ is defined in equation (B2) and plotted in Fig. B1.

4 COSMIC RAY STREAMING INSTABILITIES

The current $j_{\rm p} = n_{\rm p}e\,v_{\rm sh}$ of relativistic protons with energy $E_{\rm p}$ and a number density $n_{\rm p} = \eta_{\rm p}U_{\rm kin}/E_{\rm p}$ in equation (B3) can drive MHD turbulence due to the force $\mathbf{j_p}\times\mathbf{B}$ added in the momentum equation (Bell 2004, 2005). The parameter $\eta_{\rm p}$ represents the fraction of the kinetic energy imparted into protons with energy $E_{\rm p}$ driving the instabilities. We consider a parallel shock in the z-direction with a small perturbation in the plasma. Wave solutions $\propto \exp(ikz - \omega t)$ of the first-order MHD perturbed equations lead to the dispersion relation

$$\omega^2 = k^2v_{\rm A}^2 + \epsilon k\zeta\frac{v_{\rm sh}^2}{r_{\rm g}}(\sigma(x,s) - 1), \tag{16}$$

where $\epsilon = \pm1$,

$$\frac{r_{\rm g}}{\rm cm} \simeq 3.3\times10^{11}\left(\frac{E_{\rm p}}{\rm GeV}\right)\left(\frac{B_{\rm j}}{10\,\mu{\rm G}}\right)^{-1} \tag{17}$$

is the proton Larmor radius and $\sigma(x,s) = 0$ when $x \equiv kr_{\rm g} >> 1$ (Bell 2014). The solutions of the dispersion relation in equation (16) are plotted in Fig. 4 for $s = 2$, $v_{\rm sh} = 300$ and 1000 km s^{-1}, and $n_i = 10^3$ and 10^4 cm^{-3}. We plot Im(ω) and Re(ω) for $\epsilon = 1$ (Bell or NR branch, bottom panel) and $\epsilon = -1$ (Alfvén or resonant branch, top panel). Growing modes correspond to Im(ω) > 0. Im(ω) and Re(ω) are normalized to $1/(3t_{\rm ii})$, where $t_{\parallel} = r_{\rm g}c/3v_{\rm sh}^2$ is the time it takes a parallel shock to travel through the layer within which protons of speed $\sim c$ are confined and the upstream diffusion coefficient

Table 3. From left to right we list the source names, the relativistic electrons and protons energy power-law slope $s = 2\alpha + 1$, the total protons-to-electrons energy density ratio (a, for the case $E_{e,max} = E_{p,max} = 1$ TeV), the equipartition magnetic field (B_{eq}), the amplified field in the shock downstream region ($B_{sat,\,NR}$), the total energy density in protons ($U_{p,\,tot}$) and their acceleration efficiency ($\eta_{p,\,tot}$), the protons maximum energy ($E_{p,\,max}$), and the electrons (K_e) and protons (K_p) normalization constants. We note that $\eta_{p,\,tot}$ and $E_{p,\,max}$ are computed for $n_i = n_{\dot{M}}$ (equation 3) and $n_i = \langle n_i \rangle = \sqrt{n_{\dot{M}} n_{ff}}$ (equations 3 and 6).

	Source		s	a	B_{eq} [mG]	$B_{sat,\,NR}$ [mG]	$U_{p,tot}$ [erg cm^{-3}]	$\eta_{p,tot}$		$E_{p,max}$ [TeV]		K_e [erg^{s-1} cm^{-3}]	K_p [erg^{s-1} cm^{-3}]
								$n_i = n_{\dot{M}}$	$n_i = \langle n_i \rangle$	$n_i = n_{\dot{M}_i}$	$n_i = \langle n_i \rangle$		
(1)	G263.74	N	1.90	18.81	4.79	0.55	3.6×10^{-6}	0.43	0.07	0.13	0.04	2.5×10^{-8}	7.5×10^{-7}
(2)	G263.7759	NW	2.56	5.11	7.70	0.92	1.0×10^{-5}	0.93	0.08	0.13	0.06	4.3×10^{-10}	1.5×10^{-7}
(3)	G310.1420	A4	2.40	8.90	3.27	0.40	1.8×10^{-6}	0.86	0.06	0.38	0.14	3.1×10^{-10}	5.9×10^{-8}
(4)		D	1.92	19.24	3.65	0.42	2.1×10^{-6}	0.91	0.10	0.88	0.21	1.3×10^{-8}	4.1×10^{-7}
(5)	G313.7654	A2	2.36	10.14	2.25	0.28	8.7×10^{-7}	0.12	0.02	0.16	0.08	2.0×10^{-10}	3.3×10^{-8}
(6)		D	1.64	10.14	2.01	0.22	5.7×10^{-7}	0.08	0.06	0.65	0.26	2.0×10^{-8}	2.3×10^{-7}
(7)	G339.8838	NE	1.78	15.06	14.6	1.63	3.2×10^{-5}	0.05	0.04	0.28	0.15	4.9×10^{-7}	9.2×10^{-6}
(8)		SW	2.43	7.80	1.60	0.19	4.4×10^{-7}	0.14	0.02	0.17	0.09	5.2×10^{-11}	1.2×10^{-8}
(9)	G343.1261	N4	2.34	10.80	10.2	1.22	1.7×10^{-5}	0.13	0.03	0.17	0.09	4.8×10^{-9}	7.4×10^{-7}
(10)		S1	1.89	63.07	9.93	1.13	1.5×10^{-5}	0.20	0.06	0.43	0.16	1.1×10^{-7}	3.2×10^{-6}
(11)	G114.0853	B	1.84	17.13	0.82	0.09	1.0×10^{-7}	0.35	0.05	0.43	0.10	1.1×10^{-9}	2.5×10^{-8}
Average values			2.13		5.52	0.19	7.7×10^{-6}	0.38	0.05	0.55	0.20	3.8×10^{-9}	2.4×10^{-7}
			Section 3				Section 5			Section 6		Section 7	

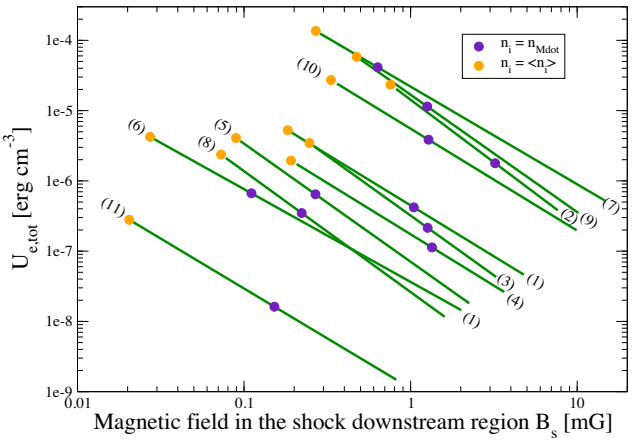

Figure 3. Non-thermal electron energy density ($U_{e,tot}$) needed to explain the synchrotron flux at the observed frequency ν in the sources listed in Table 3. The magnetic field strength in the synchrotron emitter is $B_s \leq B_{eq}$. The orange and violet circles indicate the values of $U_{e,tot}$ and B_s that satisfy the condition $U_{nt} = U_{kin}$.

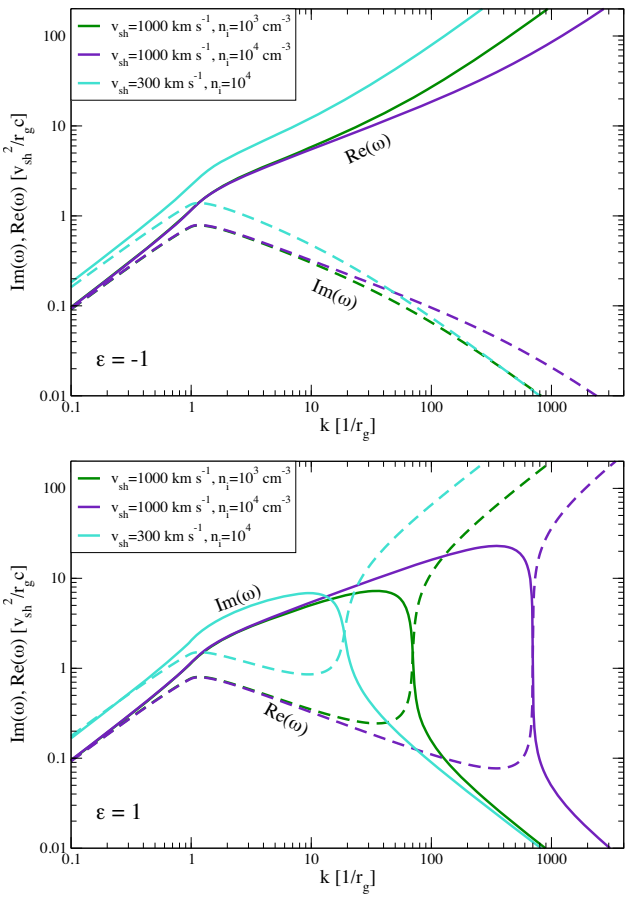

Figure 4. Dispersion relation $\omega(k)$ for the resonant (upper and lower panels for $kr_{gm} \leq 1$) and non-resonant (lower panel only for $kr_{gm} \geq 1$) modes destabilized by CRs following a power-law energy distribution with $s = 2$. Re(ω) – dashed lines – and Im(ω) – solid lines – are plotted for $v_{sh} = 300$ and 1000 km s^{-1} and $n_i = 10^3$ and 10^4 cm^{-3}. We fix $B_j = 10$ μG and $\eta_p = 0.01$.

is $\kappa_{Bohm} = r_g c/3$ (Bohm diffusion). More generally, this layer is controlled by the upstream diffusion coefficient κ_u which depends on the shock obliquity and we define the advection time as $t_{adv} = \kappa_u / v_{sh}^2$ (see Section 4.1).

We can see in Fig. 4 (top panel) that resonant waves are unstable when $kr_g \approx 1$ and therefore this instability is resonant. On the other hand, the bottom panel shows that in the NR regime ($kr_g > 1$) Im(ω) $\gg$ Re(ω) and then the NR mode is almost purely growing. The maximum growth rate $\Gamma_{max} \equiv \max(\mathrm{Im}(\omega))$ moves to the resonant regime ($kr_g \approx 1$) when v_{sh} decreases. However, even when v_{sh} is as small as 300 km s^{-1}, the NR mode is still dominant due to the large ion density of protostellar jets. Both modes are present in the plasma, although the dominance of one over the other depends on the competition between the Alfvén (that contains v_A) and the driving (that contains ζ) terms in equation (16). We note that the NR mode exists when $1/r_g \leq k \leq k_{max}$, where $k_{max} = \Gamma_{max}/v_A$. Therefore, the condition for the growth of the NR mode is $k_{max} r_g > 1$, which can

be written as $\zeta M_{\rm A}^2 > 1$, where

$$\zeta M_{\rm A}^2 \simeq 3072 \left(\frac{\eta_{\rm p}}{0.02}\right) \left(\frac{n_i}{10^4\,{\rm cm^{-3}}}\right) \left(\frac{B_{\rm j}}{10\,\mu{\rm G}}\right)^{-2} \left(\frac{v_{\rm sh}}{1000\,{\rm km\,s^{-1}}}\right)^{3}. \tag{18}$$

It is clear from equation (18) that the NR mode is more easily triggered by the fastest shocks. The condition $\zeta M_{\rm A}^2 > 1$ can be written also as $U_{\rm p}(v_{\rm sh}/c) > B_{\rm j}^2/(8\pi)$, or equivalently

$$\frac{U_{\rm p}}{{\rm erg\,cm^{-3}}} > 1.2 \times 10^{-9} \left(\frac{B_{\rm j}}{10\,\mu{\rm G}}\right)^{-2} \left(\frac{v_{\rm sh}}{1000\,{\rm km\,s^{-1}}}\right)^{-1}. \tag{19}$$

In the limit $\zeta M_{\rm A}^2 > 1$, the NR instability dominates. In the regime $k_{\rm max,\,NR} \geq k \geq 1/r_{\rm g}$, $\sigma \approx 0$ and the dispersion relation in equation (16) reduces to

$$\omega^2 = k^2 v_A^2 - k\zeta \frac{v_{\rm sh}^2}{r_{\rm g}}. \tag{20}$$

The maximum growth rate of the NR instability excited by protons with energy $E_{\rm p}$ and carrying a current of strength $j_{\rm p}$ is $\Gamma_{\rm max} = 0.5(j_{\rm p}/c)\sqrt{\pi/n_{\rm i}\,m_{\rm i}}$, giving

$$\frac{\Gamma_{\rm max,NR}}{{\rm s^{-1}}} \simeq 2.6 \times 10^{-5} \left(\frac{\eta_{\rm p}}{0.02}\right) \left(\frac{v_{\rm sh}}{1000\,{\rm km\,s^{-1}}}\right)^{3} \times \left(\frac{n_i}{10^4\,{\rm cm^{-3}}}\right)^{\frac{1}{2}} \left(\frac{E_{\rm p}}{\rm GeV}\right)^{-1}. \tag{21}$$

We note that $\Gamma_{\rm max,\,NR}$ is independent of $B_{\rm j}$, however the wavenumber $k_{\rm max,NR} = \Gamma_{\rm max,NR}/v_{\rm A} = \zeta M_{\rm A}^2/r_{\rm g}$ of the fastest growing modes does depend on $B_{\rm j}$ (see equation 18). We also note that as $\Gamma_{\rm max,\,NR}$ and $k_{\rm max,\,NR}$ decrease with $v_{\rm sh}$. Resonant modes should take over as it is the case in low-mass YSOs (Padovani et al. 2016).

In the limit $\zeta M_A^2 < 1$, the Alfvén instability dominates and the dispersion relation in equation (16) reduces to $\omega^2 = k^2 v_A^2$. The maximum growth rate of resonant modes occurs for parallel propagating modes (Achterberg 1981) at $k_{\rm max,R} \approx \sqrt{3}/r_{\rm g}$ and therefore $k_{\rm max,\,R} r_{\rm g} \approx 1$, as shown in Fig. 4 (top panel). The growth rate reaches its maximum value at $\Gamma_{\rm max,\,R} \sim \Gamma_{\rm max,\,NR}$ (e.g. Pelletier, Lemoine & Marcowith 2006; Amato & Blasi 2009). Alfven instabilities dominates over Bell instabilities when

$$\frac{v_{\rm sh}}{\rm km\,s^{-1}} < 128 \left(\frac{\eta_{\rm p}}{0.02}\right)^{-\frac{1}{2}} \left(\frac{B_{\rm j}}{10\,\mu{\rm G}}\right) \left(\frac{n_i}{10^4\,{\rm cm^{-3}}}\right)^{-\frac{1}{2}}. \tag{22}$$

This regime was studied by Padovani et al. (2015, 2016) in the context of low-mass protostars, where the jet typical velocities are $\sim$100 km s^{-1}. The important aspect of destabilizing perturbations in resonance with CRs, i.e. when $kr_{\rm g} \approx 1$, is that the scattering process is more efficient. However, this does not guarantee to have a strong amplification. In this paper, we mostly focus on the NR instability.

4.1 Magnetic field obliquity

In the perpendicular shock case, the wave speed in equation (20) now includes a contribution of the compression modes characterized by the local sound speed $c_{\rm s}$ (Bell 2005; Marcowith et al. 2018). If $c_{\rm s} < v_{\rm A}$ the non-resonant growth rate is unmodified (Bell 2005; Matthews et al. 2017). If $c_{\rm s} > v_{\rm A}$ the growth rate drops because of thermal effects (see Section 4.2.1).

The necessary condition for the streaming instabilities to grow is also modified. In perpendicular shocks, the precursor size is shorten because the particle transport is controlled by the perpendicular diffusion $\kappa_{\rm u} = \kappa_\perp = \kappa_{\rm Bohm}\kappa/(1+\kappa^2)$ (Forman & Gleeson 1975) where $\kappa = \kappa_{\rm ||}/\kappa_{\rm Bohm}$. If angular diffusion proceeds at a smaller rate than Bohm then $\kappa \gg 1$ and $\kappa_\perp \simeq \kappa_{\rm Bohm}/\kappa$. We derive the general expression $\Gamma_{\rm max,\,NR} t_{\rm adv} \sim \eta_{\rm p}(v_{\rm sh}/v_{\rm A})\kappa^b/24$, where $b = 1$ and -1 (with $\kappa > 1$) for parallel and perpendicular shocks, respectively. In perpendicular shocks, $\Gamma_{\rm max,\,NR} t_{\rm adv} > 1$ gives $\eta_{\rm p} > \kappa/M_{\rm A}$. High κ values probably quench the development of fast streaming instabilities in the configuration of a weakly CR modified shock. In the mean time, if $\kappa > 100$ then $\eta_{\rm p} > 0.1$ and the destabilization of streaming instabilities occurs in the regime of strongly CR modified shocks, a case beyond the scope of the present linear analysis.

4.2 Reduction of the NR growth rate due to environmental conditions

Different effects may reduce the growth rate of the NR instability. In this paper, we discuss thermal effects and ion-neutral collisions in non-completely ionized jets.

4.2.1 Thermal effects

Thermal effects are important when $(v_{\rm A}/v_i)^3 < (n_{\rm p}/n_i)(v_{\rm sh}/v_i)$, where the ion speed is $v_i^2 = k_{\rm B}T_{\rm u}/m_{\rm p}$ (Zweibel & Everett 2010). This leads to the condition

$$\frac{T_{\rm u}}{\rm K} > 1.1 \times 10^4 \left(\frac{\eta_{\rm p}}{0.02}\right)^{-1} \left(\frac{E_{\rm p}}{\rm GeV}\right) \times \left(\frac{v_{\rm sh}}{1000\,{\rm km\,s^{-1}}}\right)^{-3} \left(\frac{B_{\rm j}}{10\,\mu{\rm G}}\right)^{3} \left(\frac{n_i}{10^4\,{\rm cm^{-3}}}\right)^{-\frac{3}{2}} \tag{23}$$

in which case an extra term $\propto k^2 T_{\rm u}^2 r_{\rm g}\omega$ needs to be added in the dispersion relation in equation (16). The maximum growth rate of the thermally modified Bell instability is

$$\Gamma_{\rm max,th} \simeq \omega_{\rm ci} \left(\frac{n_{\rm p}}{n_{\rm i}}\right)^{\frac{2}{3}} \left(\frac{v_{\rm sh}}{v_i}\right)^{\frac{2}{3}}, \tag{24}$$

where $\omega_{\rm ci} = eB_{\rm j}/(m_{\rm p}c)$ is the ion cyclotron frequency (Reville et al. 2007). For typical values in protostellar jets,

$$\frac{\Gamma_{\rm max,th}}{\Gamma_{\rm max,NR}} \simeq 1.9 \left(\frac{\eta_{\rm p}}{0.02}\right)^{-\frac{1}{3}} \left(\frac{E_{\rm p}}{\rm GeV}\right)^{\frac{1}{3}} \left(\frac{T_{\rm u}}{10^4\,{\rm K}}\right)^{-\frac{1}{3}} \times \left(\frac{v_{\rm sh}}{1000\,{\rm km\,s^{-1}}}\right)^{-1} \left(\frac{B_{\rm j}}{10\,\mu{\rm G}}\right) \left(\frac{n_i}{10^4\,{\rm cm^{-3}}}\right)^{-\frac{1}{2}}. \tag{25}$$

We stress that $\Gamma_{\rm max,\,th} < \Gamma_{\rm max,\,NR}$ when the temperature is within the range where the condition in equation (23) is satisfied. The thermally modified Bell instability is damped when $\Gamma_{\rm max,\,th} t_{\rm adv} < 1$, i.e. when

$$\frac{T_{\rm u}}{\rm K} > 4.5 \times 10^7 \left(\frac{\eta_{\rm p}}{0.02}\right)^{2} \left(\frac{E_{\rm p}}{\rm GeV}\right), \tag{26}$$

where we have assumed $t_{\rm adv} = t_{\rm ||}$. When thermal effects are taken into account, they can reduce the growth rate of the NR instability but we do not expect strong damping by thermal effects over the development of the NR streaming modes, unless the proton acceleration efficiency $\eta_{\rm p}$ is unreasonably small in which case the NR modes are not destabilized.

4.2.2 Partially ionized medium

In a partially ionized protostellar jet (i.e. $X_{\rm u} < 1$) the friction arising between charged and neutral particles can quench the growth of CR-driven instabilities at shock precursors, and therefore DSA is less

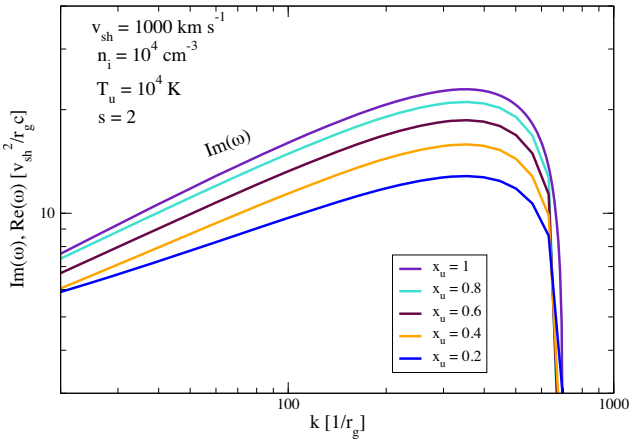

Figure 5. Growth rate for different values of the ionization fraction upstream of the shock.

efficient (e.g. Drury et al. 1996; Reville et al. 2007). When ion-neutral collisions are taken into account in the MHD equations, the dispersion relation of the CR-driven instability becomes

$$\omega^3 + i\omega^2\nu_{\rm in}\left(\frac{1}{1-X_{\rm u}}\right) + \omega\left(\epsilon\zeta\frac{v_{\rm sh}^2}{r_{\rm gm}}k(1-\sigma) - k^2v_{\rm A}^2\right) + i\nu_{\rm in}\left(\frac{X_{\rm u}}{1-X_{\rm u}}\right)\left(\epsilon\zeta\frac{v_{\rm sh}^2}{r_{\rm gm}}k(1-\sigma) - k^2v_{\rm A}^2\right) = 0, \quad (27)$$

where the ion-neutral collision frequency is given by

$$\frac{\nu_{\rm in}}{\rm s^{-1}} \simeq 8.9\times10^{-4}\left(\frac{T_{\rm u}}{10^4\ \rm K}\right)^{0.5}\left(\frac{n_{\rm n}}{10^5{\rm cm^{-3}}}\right), \quad (28)$$

in the shock upstream region with $T_{\rm u} > 140$ K and neutral density $n_{\rm n} = (1/X_{\rm u} - 1)n_i$ (Jean et al. 2009). We point out that in a completely ionized plasma $X_{\rm u} = 1$, $n_{\rm n} = 0$, and then $\nu_{\rm in} = 0$. In such a case the dispersion relation in equation (27) is identical to equation (16). We solve equation (27) for $\epsilon = 1$ and different values of $X_{\rm u}$. As pointed out by Reville et al. (2007), ion-neutral collisions are unable to stabilize the Bell modes although the maximum growth rate decreases with $X_{\rm u}$, as we illustrate in Fig. 5. This behaviour for $\Gamma_{\rm max,\,inc}$ (the maximum growth rate in the incompletely ionized jet) indicates that longer times are required to satisfy the condition $\Gamma_{\rm max,\,inc}t_{\rm adv} > 1$ to excite the NR modes.

5 MAGNETIC FIELD AMPLIFICATION

Magnetic fields in the synchrotron emitter in protostellar jets have strengths $B_{\rm s} \approx 0.1$–10 mG (see Section 3). These values are larger than the expected magnetic field in the jet termination region, $B_{\rm j} \approx$ 1–100 μG, requiring amplification of the magnetic field, given that compression by the shock does not produce strong enough fields. In this study, we consider the magnetic field amplification by the Bell instability discussed in the previous section, but in the non-linear case (Bell 2004, 2005).

In the linear regime analyzed in Section 4, the magnetic field increases exponentially with time until it reaches a value $B \sim 2B_{\rm j}$, after that the amplification enters in a non-linear regime and the magnetic field growth becomes linear with time. At a particle energy $E_{\rm p}$, the amplified magnetic field saturates at

$$\frac{B_{\rm p}^2}{8\pi} \sim \eta_{\rm p}\frac{n_{\rm i}m_{\rm i}v_{\rm sh}^3}{c} = U_{\rm p}\left(\frac{v_{\rm sh}}{c}\right) \quad (29)$$

(Bell 2004; Pelletier et al. 2006; Zirakashvili & Ptuskin 2008). The above expression refers to magnetic field amplification by protons with energy $E_{\rm p}$. However, the distribution of relativistic protons driving the current spans from $\approx$1 GeV to $E_{\rm p,\,max} \approx 1$ TeV (see Section 6) and therefore the (total) saturated magnetic field $B_{\rm sat,\,NR}$ immediately upstream of the shock is better estimated by considering the total proton population with energy density $U_{p,\rm tot}$ and acceleration efficiency $\eta_{p,\rm tot}$, which gives

$$\frac{B_{\rm sat,NR}}{\rm mG} \approx 0.3\left(\frac{U_{\rm p,tot}}{10^{-6}\,\rm erg\,cm^{-3}}\right)^{\frac{1}{2}}\left(\frac{v_{\rm sh}}{1000\,\rm km\,s^{-1}}\right)^{\frac{1}{2}} \approx 1.2\left(\frac{\eta_{\rm p,tot}}{0.1}\right)^{\frac{1}{2}}\left(\frac{n_i}{10^4\,\rm cm^{-3}}\right)^{\frac{1}{2}}\left(\frac{v_{\rm sh}}{1000\,\rm km\,s^{-1}}\right)^{\frac{3}{2}}. \quad (30)$$

We note that $B_{\rm sat,\,NR}$ does not depends on $B_{\rm j}$.

Once the magnetic field strength reaches the saturation value $B_{\rm sat,\,NR}$, the Alfvén velocity becomes larger and $\eta_{\rm p}M_{\rm A}^2$ decreases. At the same time the Larmor radius of particles decreases down to values $r_g \sim 1/k$ and then the NR Bell instability becomes subdominant. Caprioli & Spitkovsky (2014b) proposed a refined model for the growth of the non-resonant modes including a non-linear stage (when energy densities in the turbulent and background magnetic fields become similar). They find a maximum magnetic field strength $B_{\rm max}/B_{\rm j} \sim M/\sqrt{2}$, where $M = v_{\rm sh}/c_{\rm s}$ is the sonic Mach number and $c_{\rm s}$ is the sound speed. In our case we have moderate M with a typical range 5–50, which makes the result obtained in equation (30) likely optimistic. It should be also noted that Caprioli & Spitkovsky (2014b) conduct their study in the regime of beta plasma parameter $\beta_{\rm p} = 2(c_{\rm s}/v_{\rm A})^2 \sim 1$, whereas MYSO jets have rather $\beta_{\rm p} > 1$ if not $\gg$1 because they are relatively hot and dense with a weak magnetic field.

5.1 The magnetic field in the shock downstream region

The perturbations produced by the NR instability can lead to various effects in the shock downstream region (Giacalone & Jokipii 2007). As NR modes are not normal modes of the plasma, they are expected to be damped rapidly once the source of excitation disappears. Weibel instabilities would also contribute to produce magnetic field fluctuations upstream of the shocks. However, Weibel modes are expected to decay over a few plasma skin depth downstream, so over much smaller scales than $R_{\rm j}$. Conversely, dynamo processes can further amplify the magnetic field produced at the shock front (Bell 2004; Pelletier et al. 2006; Inoue, Yamazaki & Inutsuka 2009; Marcowith & Casse 2010; Tzeferacos et al. 2018; van Marle, Casse & Marcowith 2018), even if the upstream region is partially ionized (Xu & Lazarian 2017). This aspect involves a model of non-linear evolution of the plasma and it is beyond the scope of this paper. For simplicity, we consider that the amplified magnetic field in the shock upstream region is compressed by the shock and maintained on a spatial scale $\sim R$ (the size of the synchrotron emitter).

In the shock downstream region, the (turbulent) isotropic upstream random magnetic field is compressed by the shock by a factor $r_{\rm B} = \sqrt{(2r^2+1)/3} \approx 3.3$ when the shock compression ratio is $r = 4$ (e.g. Parizot et al. 2006; Zirakashvili & Ptuskin 2008).[8] Therefore, the amplified field downstream of the shock is $B_{\rm sat,\,d} = r_{\rm B}B_{\rm sat,\,NR}$. On the other hand, the magnetic field in the synchrotron emitter $B_{\rm s}$, i.e. mostly coming from the shock downstream region, is a function of the energy density in non-thermal electrons. In Fig. 6, we plot $U_{\rm p,\,tot} =$

[8]Hereafter, we use $r = 4$ and $r_{\rm B} = 3.3$.

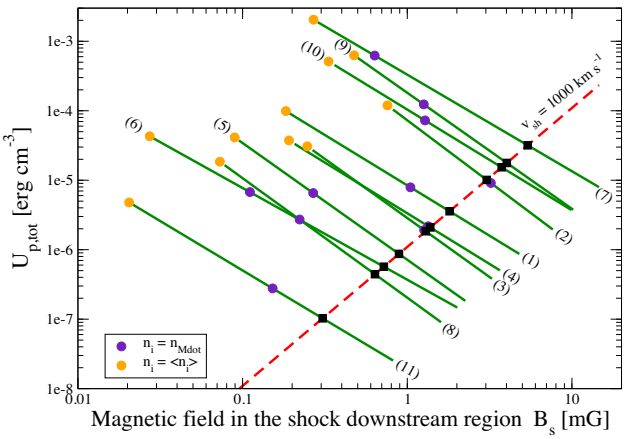

Figure 6. Non-thermal protons energy density ($U_{\rm p,tot} = aU_{\rm e,tot}$) needed to explain the synchrotron flux at the observed frequency ν in the sources listed in Table 3 (green solid lines). The magnetic field strength in the synchrotron emitter is $B_{\rm s} \leq B_{\rm eq}$, as in Fig. 3. The red dashed line represents the energy density in non-thermal protons needed to amplify the magnetic field up to the saturation value $B_{\rm sat,\,NR}$ as indicated in equation (30). The black squares indicate the value of the magnetic field when $v_{\rm sh} = 1000$ km s^{-1}. The orange and violet circles indicate the values of $U_{p,\rm tot}$ and $B_{\rm s}$ that satisfy the condition $U_{\rm nt} = U_{\rm kin}$.

$aU_{\rm e,\,tot}$ (green solid lines), where $U_{\rm e,\,tot}$ is given by equation (13), and $U_{\rm p,tot} = (c/v_{\rm sh})B^2_{\rm sat,NR}/(8\pi)$ by equation (30) (red dashed line). By assuming that $B_{\rm sat,\,d} = B_{\rm s}$, we find that

$$\frac{B_{\rm sat,d}}{B_{\rm eq}} = \left[r_{\rm B}^2\left(\frac{a}{1+a}\right)\left(\frac{v_{\rm sh}}{c}\right)\right]^{\frac{2}{s+5}} \sim 0.38\xi_{\rm sat}(s)\left(\frac{v_{\rm sh}}{1000\,{\rm km\,s^{-1}}}\right)^{\frac{2}{s+5}} \quad (31)$$

and

$$\frac{U_{\rm p,tot}}{\rm erg\,cm^{-3}} = 1.7\times10^{-6}\xi_{\rm sat}^2\left(\frac{v_{\rm sh}}{1000\,{\rm km\,s^{-1}}}\right)^{-\frac{s+1}{s+5}}\left(\frac{B_{\rm eq}}{\rm mG}\right)^2, \quad (32)$$

where $\xi_{\rm sat} = 10^{0.42(s-2)/(s+5)}$ (see Fig. A1) and we have fixed $r_{\rm B} = 3.3$ and $a/(1+a) \sim 1$. In Fig. 6, we indicate $B_{\rm s}$ and $U_{\rm p,tot}$ for the cases with $v_{\rm sh} = 1000$ km s^{-1} (black squares). In Table 3, we list $B_{\rm sat,\,NR} = B_{\rm s}/3.3$ and $U_{\rm p,tot}$ for $v_{\rm sh} = 1000$ km s^{-1}. We list also $\eta_{\rm p,tot} = U_{\rm p,tot}/U_{\rm kin}$ for $n_i = n_{\dot{M}}$ and $\langle n_i\rangle$. We remark that sources G263.7759 NW (2) and G310.1420 A4,D (3,4) have $\eta_{\rm p,tot} \sim 1$ when $B_{\rm s} = 3.3B_{\rm sat,\,NR}$, $n_i = n_{\dot{M}}$ and $v_{\rm sh} = 1000$ km s^{-1}. Therefore, we conclude that in these sources the magnetic field either cannot be amplified by Bell instabilities or $n_i > n_{\dot{M}}$.

Contrary to the case of supernova remnants where the magnetic field in the shock downstream region is calculated from the synchrotron cooling length of X-ray-emitting electrons, in the non-thermal lobes considered in this study the radio-emitting electrons are not in the fast cooling regime. We have therefore estimated the magnetic field in the non-thermal hotspots by assuming that upstream of the shock the magnetic field is amplified by the Bell's instability up the the saturation regime given by equation (30) and by equating $B_s = 3.3B_{\rm sat,\,NR}$. By assuming that the downstream magnetic field is $B_{\rm s} = B_{\rm sat,\,d} = 3.3B_{\rm sat,\,NR}$ we determine $B_{\rm s}$, $U_{\rm p,tot}$, and $\eta_{\rm p,tot}$. Once we know the protons acceleration efficiency and the magnetic field, we compute in the following sections the maximum energy of particles (Section 6) and the γ-ray emission (Section 7), respectively.

6 MAXIMUM ENERGIES

6.1 Protons

If the non-resonant streaming instability is important and the magnetic field is amplified, the maximum energy of protons is determined by the amount of protons that escape from the shock upstream region (Zirakashvili & Ptuskin 2008; Bell et al. 2013). Given that only the most energetic protons can penetrate far upstream from the shock and amplify the magnetic field in the shock precursor, the available time to accelerate these particles is $\sim 5/\Gamma_{\rm max,\,NR}(E_{\rm p,\,max})$, where $\Gamma_{\rm max,\,NR}(E_{\rm p,\,max})$ is the maximum growth rate of NR modes driven by protons with an energy $E_{\rm p,\,max}$. By equating $5/\,\Gamma_{\rm max,NR}(E_{p,\rm max}) = R_{\rm j}/v_{\rm sh}$ and using equation (B3) with $E_{\rm p} = E_{\rm p,\,max}$ we find

$$\frac{E_{\rm p,max}}{\rm m_p c^2} = \begin{cases} (2-s)F & s<2 \\ \log\left(\frac{E_{\rm p,max}}{\rm GeV}\right)^{-1} F & s=2 \\ \left[(s-2)\frac{1}{m_{\rm p}c^2}F\right]^{\frac{1}{s-1}} & s>2 \end{cases} \quad (33)$$

(Bell et al. 2013; Schure & Bell 2014), where

$$F \simeq 65.83\left(\frac{U_{\rm p,tot}}{10^{-5}\,{\rm erg\,cm^{-3}}}\right)\left(\frac{R_{\rm j}}{10^{16}\,{\rm cm}}\right)\left(\frac{n_i}{10^4\,{\rm cm^{-3}}}\right)^{-\frac{1}{2}}. \quad (34)$$

Values of $E_{\rm p,\,max}$ for the non-thermal lobes in our study are listed in Table 3 for the case $v_{\rm sh} = 1000\,{\rm km\,s^{-1}}$ and $R_{\rm j} = R/2$. We also considered $n_i = n_{\dot{M}_i}$ and $\langle n_i\rangle$. Notice that around the shock the proton mean free path is $\kappa r_{\rm g}$. Unless $\kappa \gg 1$, this mean free path at $E_{\rm p,\,max}$ is always much smaller than $R_{\rm j}$. The condition $\Gamma_{\rm max,\,NR}(E_{\rm p,\,max})R_{\rm j}/v_{\rm sh} > 5$ was introduced by Bell et al. (2013) for the case of SNR and where they considered the size of the spherical shock (instead of $R_{\rm j}$). However, Zirakashvili & Ptuskin (2008) found a similar expression for planar non-relativistic shocks. We also note that the same limit applies when Alfvén waves dominate given that the maximum growth rate is almost the same (Zirakashvili & Ptuskin 2008).

For large temperatures or low magnetic fields (see equation 23), thermal effects are important and therefore $E_{\rm p,\,max}$ is obtained by equating $5/\Gamma_{\rm max,\,th} = R_{\rm j}/v_{\rm sh}$. If the jet is not completely ionized, the maximum energy of protons due to escape upstream is reduced by a factor $(\Gamma_{\rm max,\,inc}/\Gamma_{\rm max,\,NR})^{1/(s-1)}$.

6.2 Electrons

Previous models consider Alfvén turbulence and Bohm diffusion (see e.g. Araudo et al. 2007; Bosch-Ramon et al. 2010; Padovani et al. 2015, 2016). In this study, electrons diffuse in the turbulence self-generated by protons. They are not the main drivers of the turbulence and can be considered as test particles. If the non-resonant streaming instability gets into the non-linear phase, and possibly other instability can contribute to generate longer wavelength perturbations, we can expect to have the turbulence coherence length $\ell_{\rm c}$ limited by the Larmor radius of the protons at the maximum energy $E_{\rm p,\,max}$ in the amplified field $B_{\rm s}$ (see the discussion in e.g. Reville, Kirk & Duffy 2009; Caprioli & Spitkovsky 2014b).

If at first we assume that the maximum electrons energy $E_{\rm e,\,max}$ exceeds $E_{\rm p,\,max}$, then the turbulence experienced by electrons will be in the small-scale turbulence regime and the diffusion coefficient would be $\kappa_{\rm u} \simeq \kappa D_{\rm Bohm}(E_{\rm p,max}, B_{\rm s})(E_{\rm e}/E_{\rm p,max})^2$. This rapid increase with the energy would limit $E_{\rm e,\,max}$ to $E_{\rm p,\,max}$ unless radiative losses dominate and limit it to smaller values. Then, one should expect to have $E_{\rm e,\,max} \leq E_{\rm p,\,max}$.

By inserting $\kappa_{\rm u}$ into the acceleration time-scale ($t_{\rm acc} \propto \kappa_{\rm u}/v_{\rm sh}^2$) and the diffusive loss time-scale ($R_{\rm j}^2/6\kappa_{\rm u}$) we find a maximum electron

energy $E_{\rm e,\,max,\,diff}$ to be within a factor of a few of the maximum electron energy fixed by synchrotron losses $E_{\rm e,\,max,\,rad}$ for the different sources in our sample. Then, one can argue that the statement $E_{\rm e,\,max} \leq E_{\rm p,\,max}$ is reasonably verified accounting for the uncertainties on the parameters controlled by the microphysics of turbulence generation at fast shocks, namely $\ell_{\rm c}, \kappa, B_{\rm s}$, and on the macroscopic jet parameters $v_{\rm sh}$ and $R_{\rm j}$. Hereafter, we assume that $E_{\rm e,\,max} = E_{\rm p,\,max}$ ($E_{\rm e,\,max,\,rad} < E_{\rm p,\,max}$ never happens in our source sample with the derived values of the magnetic field strength $B_{\rm s}$.) We left to a future work more precise calculation of $E_{\rm e,\,max}$.

7 GAMMA-RAY EMISSION

TeV electrons and protons can emit gamma-rays by their interaction with ambient cold protons through relativistic bremsstrahlung and proton–proton (pp) collisions. Inverse Compton scattering is a mechanism contributing to gamma-ray emission as well. In the jet termination region, at $\sim 10^4$ au from the central protostar, the stellar photon field is very diluted and therefore the Inverse Compton scattering is not expected to be very relevant. However, we stress that thermal photons from the bow-shock downstream region can be boosted to the γ-ray domain. The γ-ray flux by upscattering of photons from the bow shock will be computed in a following paper, together with the diffuse emission in the molecular cloud.

Proton–proton and relativistic bremsstrahlung cooling time-scales are comparable. However, the number of relativistic protons per unit energy is larger than that of electrons, i.e. $N_{\rm p} > N_{\rm e}$, given that $K_{\rm p} > K_{\rm e}$ (see Appendix B and Fig. A1) and we assume that the slope is the same in both electrons and protons energy distributions. In particular, the distribution of relativistic protons in the jet hotspot is $N_{\rm p} = K_{\rm p} E_{\rm p}^{-s}$, where $K_{\rm p} = K_{\rm e}(m_{\rm p}/m_{\rm e})^{(s-1)/2}$ and K_e is computed from equation (A5) by fixing $B_{\rm s} = 3.3 B_{\rm sat,\,NR}$. In Table 3, we list the values of $K_{\rm e}$ and $K_{\rm p}$. As a consequence, the emission in the γ-ray domain will be dominated by hadrons.

7.1 Proton–proton collisions

In the one-zone model approximation, the specific luminosity of gamma-rays due to π^0-decay can be written as

$$E_\gamma L_{\gamma,pp} = E_\gamma^2 \, q_\gamma(E_\gamma) \, n_{\rm lobe} \, V_{\rm e}, \tag{35}$$

where q_γ is the emissivity (see equations 16 and 17 in Araudo et al. 2007). We assume that the volume of the γ-ray emitter is the same as the synchrotron emission volume ($V_{\rm e}$) and that the thermal ion density in the lobe is $n_{\rm lobe} = 4 n_{\dot{M}}$. In Fig. 7, we plot the flux $F_{\gamma,\rm pp} = E_\gamma L_{\gamma,\rm pp}/(4\pi d^2)$ for all the sources from our sample and the *Fermi*-LAT sensitivity. We can see that the predicted emission in G339-8838 NE (7), G34301261 N4 (9), and S1 (10) is detectable by *Fermi*-LAT after 10 yr of observation (with 5σ-confidence) when $n_{\rm lobe} = 4 n_{\dot{M}}$. For these three sources we plot in Fig. 8 the spectral energy distribution (SED) including also synchrotron emission and relativistic bremsstrahlung and using the formulation in Blumenthal & Gould (1970). We assume $E_{\rm e,max} = E_{\rm p,max}$ as it is calculated in equation (33).

We note that $F_{\gamma,\,pp} \propto n_{\rm lobe}$ and therefore the interaction of relativistic protons with clumps denser than the jet will increase the γ-ray flux.

7.2 Density enhancement in the jet termination region

The termination region of non-relativistic light jets ($n_{\rm j} < n_{\rm mc}$) is expected to be a combination of an adiabatic reverse shock and a radiative bow shock, leading to a large density ratio at the contact discontinuity between both shocks (see e.g. Rodríguez-Kamenetzky et al. 2019). The density of the plasma downstream of the radiative bow shock is

$$\frac{n'_{\rm mc}}{n_{\rm mc}} = 500 \left(\frac{v_{\rm bs}}{100\,{\rm km\,s^{-1}}}\right)^2 \left(\frac{T}{10^4 {\rm K}}\right)^{-1} \tag{36}$$

(e.g. Blondin et al. 1990) when the plasma is cooled down to a temperature T, making the density contrast at the contact discontinuity $\chi' = 4 n_{\rm j}/n'_{\rm mc} \ll \chi$. As a consequence, the contact discontinuity is unstable to dynamical and thermal instabilities. A dense layer of density $n'_{\rm mc}$ located at distance $l_{\rm th}$ downstream of the bow shock (see equation 1) fragments into several clumps (e.g. Calderón et al. 2020). In this case, the effective density downstream the reverse shock will increase up to a value $\sim f_{\rm v,clump} n'_{\rm mc}$, where $f_{\rm v,\,clump} \leq 1$ is the volume-filling factor of clumps in the lobe with volume $\sim R_{\rm j}^3$. However, we draw attention to the fact that the component of the magnetic field in the ambient molecular cloud parallel to the bow shock front ($B_{\rm mc,\perp}$) limits the compression factor to a maximum value (Blondin et al.

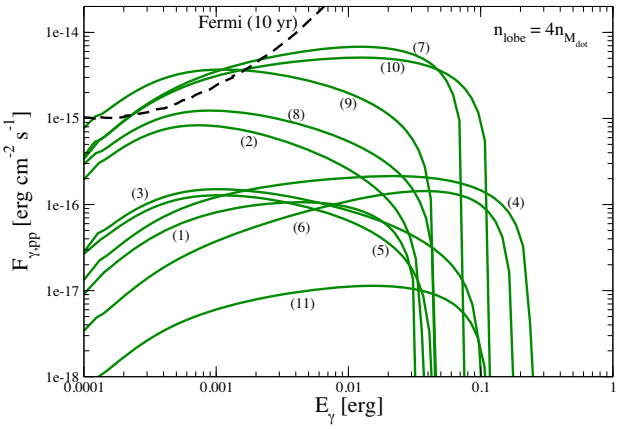

Figure 7. π^0-decay for all the sources in our sample for the case of $n_i = n_{\dot{M}}$. The black dashed lines indicates the *Fermi* sensitivity for 10 yr of observation. The numbers indicate the source name (see Table 3).

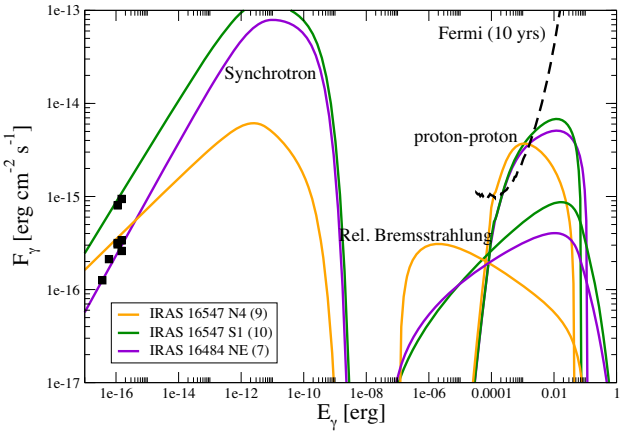

Figure 8. SED from radio to gamma-rays for the three hot spots: IRAS 16547 N4, IRAS 16547 S1, and IRAS 16848 NE. The black squares indicate synchrotron data (Purser et al. 2016) and the black dashed line represent the *Fermi* sensitivity for 10 yr of observation.

1990)

$$\frac{n'_{\rm max}}{n_{\rm mc}} \sim 100 \left(\frac{n_{\rm mc}}{10^4\,{\rm cm^{-3}}}\right)^{\frac{1}{2}} \left(\frac{v_{\rm bs}}{100\,{\rm km\,s^{-1}}}\right) \left(\frac{B_{\rm mc,\perp}}{0.1{\rm mG}}\right)^{-1}. \quad (37)$$

The magnetic field in molecular clouds is $B_{\rm mc} \sim$ mG (Crutcher 2012) and we have assumed that $B_{\rm mc,\perp} \sim 0.1 B_{\rm mc}$. In the case of light jets, $v_{\rm bs} \sim v_{\rm j}\sqrt{\chi} = v_{\rm j}\sqrt{n_{\rm j}/n_{\rm mc}}$ (see Section 2.2) and therefore equation (37) can be written as

$$\frac{n'_{\rm max}}{n_{\rm mc}} \sim 1000 \left(\frac{n_{\rm j}}{10^4\,{\rm cm^{-3}}}\right)^{\frac{1}{2}} \left(\frac{v_{\rm j}}{1000\,{\rm km\,s^{-1}}}\right) \left(\frac{B_{\rm mc,\perp}}{0.1\,{\rm mG}}\right)^{-1}. \quad (38)$$

This indicates that significant enhancement in the plasma density downstream of the reverse shock is feasible if instabilities grow fast enough to fragment the dense shell and form the clumps. However, we note that even when clumps are not formed, protons accelerated at the jet reverse shock can diffuse down to the dense shell and radiate there.

7.2.1 *Kelvin–Helmholtz and Rayleigh–Taylor instabilities*

Kelvin–Helmoltz (KH) and Rayleigh–Taylor (RT) instabilities can grow in the contact discontinuity due to the velocity shear and the force exerted by the downstream material of the reverse shock on that of the bow shock. If the bow shock is radiative, the formation of a shell much denser than the jet ($n_{\rm j}$) and the molecular cloud ($n_{\rm mc}$) at the contact discontinuity makes the working surface unstable even in the case of light jets. Following the analysis in Blondin et al. (1990), the acceleration of the dense shell with a width $w_{\rm shell}$ can be written as $a \sim n_{\rm j} v_{\rm rs}^2 / n'_{\rm mc} w_{\rm shell}$. For a characteristic dynamical time-scale $t_{\rm dyn} = R_{\rm j}/v_{\rm j}$ we find

$$\frac{t_{\rm RT}}{t_{\rm dyn}} \sim 0.05 \left(\frac{T}{10^4\,{\rm K}}\right)^{-\frac{1}{2}} \left(\frac{v_{\rm j}}{1000\,{\rm km\,s^{-1}}}\right), \quad (39)$$

where $t_{\rm RT} \sim 1/\sqrt{ak}$ is the growing time of RT instabilities and we have assumed that $k \sim 1/2 w_{\rm shell}$ and $w_{\rm shell} \sim R_{\rm j}/3$.

8 SUMMARY AND CONCLUSIONS

The detection of synchrotron emission from jets powered by high-mass protostars indicates that electrons are *in situ* accelerated. We consider a sample of 11 non-thermal lobes in MYSOs as referenced by Purser et al. (2016) and Obonyo et al. (2019). From the observational data in the above-mentioned papers, the lobes selected for our study have an average radio spectral index $\alpha = 0.55$, emissivity $\epsilon_{\rm synchr} = 2.1 \times 10^{-30}$ erg cm^{-3} s^{-1} Hz^{-1}, and linear size $R = 2.9 \times 10^{16}$ cm (see Table 4). Magnetic fields $B_{\rm s} \sim 0.3$–5 mG are needed to explain the synchrotron radio flux. These large values of $B_{\rm s}$ are difficult to explain by a simple compression in an adiabatic strong shock at the jet termination region, at ∼0.1 pc from the central protostar. We note that strong compression of the magnetic field in the molecular cloud by the radiative bow shock could explain values of $B_{\rm s}$ in the range 0.3–5 mG, and this scenario will be analysed in a future study. In this paper, we focus on magnetic field amplification by streaming instabilities.

CR streaming instabilities can generate magnetic field perturbations necessary for the particles to diffuse back and forth the shock. The CR streaming can amplify resonant Alfvén waves with wavelength of the order of the CR Larmor radius $r_{\rm g}$ but also excite the NR (Bell) instability which produces perturbations at scales much smaller than $r_{\rm g}$ (Bell 2004). Bell's instability can amplify small perturbations in the magnetic field up to values much larger than the unperturbed jet magnetic field $B_{\rm j}$ if $\zeta M_{\rm A} > 1$ where

$$\zeta M_{\rm A}^2 = 7000 \left(\frac{U_{\rm p}}{10^{-7}\,{\rm erg\,cm^{-3}}}\right) \left(\frac{B_{\rm j}}{10\,\mu{\rm G}}\right)^{-2} \left(\frac{v_{\rm sh}}{1000\,{\rm km\,s^{-1}}}\right) \quad (40)$$

is an equivalent expression for equation (18). We remark that even in the case where ζ is small due to the slow speed of the shock (compared e.g. with supernova remnants), the large values of jet densities makes $M_{\rm A}$ significantly large to satisfy the condition $\zeta M_{\rm A}^2 \gg 1$ over a large range of parameters. However, large ion densities in a non-completely ionized jet would increase the ion-neutral collisions. Alfvén waves can be damped by ion-neutral collisions (e.g. Drury et al. 1996). Conversely, Bell modes are not as heavily damped, although the maximum growth rate decreases (Reville et al. 2007). Thermal effects only weakly affect the NR instability growth rate (see Fig. 5). High magnetic field obliquity can also lead to a decrease of the streaming instability growth rates or even a complete quenching if the precursor length becomes too short (see Section 4.1).

By assuming that the large magnetic field in the synchrotron emitter ($B_{\rm s}$) is due to amplification through the Bell's instability and fixing $v_{\rm sh} = 1000$ km s^{-1} we estimate $B_{\rm s} \sim 0.4 B_{\rm eq}$ and the energy density in non-thermal electrons $U_{\rm e,tot}$. Then, the energy density in non-thermal protons is $U_{\rm p,tot} = a U_{\rm e,tot}$. Under the assumption that the jet ionized density is $n_i = \langle n_i \rangle$, we estimate the proton acceleration efficiency $\eta_{\rm p,tot}$ to be ∼0.05. We stress that this method is different with respect to that used in supernova remnants, where the magnetic field is usually estimated by comparing the width of X-ray filament profiles with the synchrotron cooling length.

By knowing $\eta_{\rm p,tot}$ and $B_{\rm s}$ we estimate the maximum energy of protons accelerated in the jet reverse shock and the γ-ray emission that they produce. By considering the amplification time-scale of the magnetic field in the shock upstream region we find $E_{\rm p,max} \sim 0.1$ TeV. These protons can emit γ rays through their collisions with thermal ions. We compute the γ-ray flux $F_{\gamma,pp}$ for all the sources in our sample. We note that $F_{\gamma,pp} \propto n_{\rm lobe}$ and the jet ionized density at the termination region is $n_{\dot{M}} \leq n_i \leq n_{\rm ff}$, where $n_{\rm ff}/n_{\dot{M}} \sim 100$ (see Fig. 2). We find that having a density $n_{\rm lobe} = 4 n_{\dot{M}}$ in the non-thermal

Table 4. Average values of the most relevant parameters in our study (see Tables 2 and 3).

From observations	
Radio spectral index	$\alpha = 0.55$
Synchrotron emissivity	$\epsilon_{{\rm syn},\nu} = 2 \times 10^{-30}$ erg cm^{-3} s^{-1} Hz^{-1}
Size of the non-thermal lobe	$R = 2.9 \times 10^{16}$ cm
Assumed values	
Shock speed	$v_{\rm sh} = 1000$ km s^{-1}
Jet magnetic field	$B_{\rm j} = 10\,\mu$G
Jet temperature	$T_{\rm u} = 10^4$ K
Computed values	
Jet ion density	$n_{\rm i} = n_{\dot{M}} = 1.2 \times 10^3$ cm^{-3}
	$n_{\rm i} = \langle n_i \rangle = 1.6 \times 10^4$ cm^{-3}
Minimum shock speed	$v_{\rm sh,\,ad} = 455$ km s^{-1}
Equipartition magnetic field	$B_{\rm eq} = 7.25$ mG
Downstream magnetic field	$B_{\rm s} = 0.84$ mG
Protons total energy density	$U_{\rm p,tot} = 1.5 \times 10^{-5}$ erg cm^{-3}
Protons total acceleration efficiency	$\eta_{\rm p,tot} = 0.05$
Protons maximum energy	$E_{\rm p,max} = 0.24$ TeV
Electrons normalization constant	$K_{\rm e} = 3.8 \times 10^{-9}$ erg^{s-1} cm^{-3}
Protons normalization constant	$K_{\rm p} = 2.4 \times 10^{-7}$ erg^{s-1} cm^{-3}

emitter is high enough to reach detectable levels of γ rays with *Fermi* in IRAS 16547 N4, IRAS 16547 S1, and IRAS 16848 NE, as we show in Fig. 7. Although there is no claim of detection of these sources by *Fermi*, we expect that our result will motivate a future study on the *Fermi* data at the location of these sources. In addition, these sources will be perfect targets for a point-source mode. We also note that mixing due to dynamical instabilities can significantly enhance the density of targets in the lobes. The very dense shell formed downstream of the radiative bow shock is unstable and fragmented in clumps with density ∼100–1000 times the density of the ambient medium (i.e. the molecular cloud). By achieving $F_{\gamma,pp} \sim 5 \times 10^{-13}$ erg cm^{-2} s^{-1} at 0.1 TeV, CTA will be of great importance to measure the cut-off of the spectrum. Also, the spatial resolution of CTA is expected to be better than *Fermi*. The detection of γ rays from protostellar jets will open a new window to study stellar formation, as well as the efficiency of DSA in the high-density ($n_{\rm i} \sim 10^3$–10^4 cm^{-3}) and low-velocity ($v_{\rm sh} \sim 1000$ km s^{-1}) regime. In particular, the detection of diffuse gamma-ray emission in molecular clouds where MYSOs are embedded will be a piece of evidence of proton acceleration in protostellar jets.

In a following paper, we will perform more detailed calculations of the multiwavelength lepto-hadronic SED, from radio to γ rays. The diffuse γ-ray emission of particles accelerated in the jet termination shocks and interacting with ions in the molecular cloud where the protostar is embedded, as well as the emission of secondary particles, will be also modelled. We will select the most promising candidates from the sample of sources in this study, as well as other sources such as IRAS 18162−2048 and the powering massive protostar of the Herbig–Haro objects HH80, HH81, and HH80N (see e.g. Rodríguez-Kamenetzky et al. 2017, 2019).

High-sensitivity radio observations in the GHz domain are very important to model the synchrotron emission and constrain the energy density in non-thermal particles (Section 3). To this purpose, the detection of polarized emission will be crucial to disentangle thermal contamination in the GHz domain, as well as to investigate the morphology of the magnetic field near the shock. The Next Generation Very Large Array (ngVLA) will play a fundamental role on that (Galván-Madrid et al. 2018; Hull et al. 2018). Moving to lower frequencies, the low-energy cut-off of the electrons distribution is an important parameter related with the efficiency of shocks to inject electrons from the thermal pool to the high-energy tail. In this sense, the forthcoming Square Kilometre Array (SKA) will be extremely important to observe the low-energy cut-off (see e.g. Feeney-Johansson et al. 2019).

Finally, we note that protostellar jets have been well studied through several laboratory experiments (e.g. Nicolaï, Stenz & Kasperczuk 2008; Suzuki-Vidal, Bocchi & Lebedev 2012; Liang et al. 2018). In particular, Suzuki-Vidal et al. (2015) have shown that laboratory bow shocks formed by the collision of two counterstreaming and supersonic plasma jets is fragmented due to the rapid growth of thermal instabilities. The formation of collisionless shocks (Li, Tikhonchuk & Moreno 2019), the development of plasma instabilities, and the acceleration of particles in laser plasma (Reville, Bell & Gregori 2013) is going to open a fascinating era of laboratory astrophysics in synergy with high-energy astrophysics.

ACKNOWLEDGEMENTS

The authors thank the anonymous referee for his/her comments that helped us to improve the quality of our paper. The authors thank C. Carrasco-González and S. Cabrit for insightful discussions on protostellar jets. ATA thanks Tony Bell and K. Blundell for encouragement and motivating discussions on jets, particle acceleration, and streaming instabilities. ATA thanks M.V. del Valle and R. Santos-Lima for their help with numerical calculations. ATA thanks the Czech Science Foundation under the grant GAČR 20-19854S titled 'Particle Acceleration Studies in Astrophysical Jets'. MP acknowledges funding from the INAF PRIN-SKA 2017 program 1.05.01.88.04, by the Italian Ministero dell'Istruzione, Università e Ricerca through grant Progetti Premiali 2012–iALMA (CUP C52I13000140001), and by the project PRIN-INAF-MAIN-STREAM 2017 'Protoplanetary disks seen through the eyes of new-generation instruments'. This work has been carried out with the support of the OCEVU Labex (ANR-11-LABX-0060) and the A∗MIDEX project (ANR-11- IDEX-0001-02) funded by the 'Investissements d'Avenir' French government program managed by the ANR.

DATA AVAILABILITY

The calculations presented in this paper were performed using a private code developed and owned by the corresponding author; please contact her for any request/question about. Data appearing in the figures are available upon request.

REFERENCES

Achterberg A., 1981, A&A, 98, 161
Ackermann M. et al., 2014, Science, 345, 554
Albertazzi B. et al., 2014, Science, 346, 325
Amato E., Blasi P., 2009, MNRAS, 392, 1591
Anglada G., Rodríguez L. F., Carrasco-González C., 2018, A&AR, 26, 3
Araudo A. T., Romero G. E., Bosch-Ramon V., Paredes J. M., 2007, A&A, 476, 1289
Araudo A. T., Bell A. R., Blundell K. M., 2015, ApJ, 806, 243
Arbutina B., Urošević D., Andjelić M. M., Pavlović M. Z., Vukotić B., 2012, ApJ, 746, 79
Axford W. I., Leer E., Skadron G., 1977, Int. Cosm. Ray Conf., 11, 132
Bacciotti F., Eislöffel J., 1999, A&A, 342, 717
Beck R., Krause M., 2005, Astron. Nachr., 326, 414
Bell A. R., 1978a, MNRAS, 182, 147
Bell A. R., 1978b, MNRAS, 182, 443
Bell A. R., 2004, MNRAS, 353, 550
Bell A. R., 2005, MNRAS, 358, 181
Bell A. R., 2014, Braz. J. Phys., 44, 415
Bell A. R., Schure K. M., Reville B., Giacinti G., 2013, MNRAS, 431, 415
Blandford R. D., Ostriker J. P., 1978, ApJ, 221, L29
Blandford R. D., Payne D. G., 1982, MNRAS, 199, 883
Blondin J. M., Fryxell B. A., Konigl A., 1990, ApJ, 360, 370
Blumenthal G. R., Gould R. J., 1970, Rev. Mod. Phys., 42, 237
Bosch-Ramon V., Romero G. E., Araudo A. T., Paredes J. M., 2010, A&A, 511, A8
Calderón D., Cuadra J., Schartmann M., Burkert A., Prieto J., Russell C. M. P., 2020, MNRAS, 91
Caprioli D., Spitkovsky A., 2014a, ApJ, 783, 91
Caprioli D., Spitkovsky A., 2014b, ApJ, 794, 46
Carrasco-González C., Rodríguez L. F., Anglada G., Martí J., Torrelles J. M., Osorio M., 2010, Science, 330, 1209
Casse F., Keppens R., 2002, ApJ, 581, 988
Ceccarelli C., Dominik C., López-Sepulcre A., Kama M., Padovani M., Caux E., Caselli P., 2014, ApJ, 790, L1
Cécere M., Velázquez P. F., Araudo A. T., De Colle F., Esquivel A., Carrasco-González C., Rodríguez L. F., 2016, ApJ, 816, 64
Cerqueira A. H., de Gouveia dal Pino E. M., Herant M., 1997, ApJ, 489, L185
Chen B., Bastian T. S., Shen C., Gary D. E., Krucker S., Glesener L., 2015, Science, 350, 1238

Chernin L., Masson C., Gouveia dal Pino E. M., Benz W., 1994, ApJ, 426, 204
Combet C., Ferreira J., 2008, A&A, 479, 481
Crusius-Watzel A. R., 1990, ApJ, 361, L49
Crutcher R. M., 2012, ARA&A, 50, 29
Drury L., Duffy P., Kirk J. G., 1996, A&A, 309, 1002
Favre C. et al., 2018, ApJ, 859, 136
Fedriani R. et al., 2019, Nat. Commun., 10, 3630
Feeney-Johansson A., Purser S. J. D., Ray T. P., Eislöffel J., Hoeft M., Drabent A., Ainsworth R. E., 2019, ApJ, 885, L7
Ferrière K. M., 2001, Rev. Mod. Phys., 73, 1031
Fontani F. et al., 2017, A&A, 605, A57
Forman M. A., Gleeson L. J., 1975, Ap&SS, 32, 77
Galván-Madrid R., Beltrán M., Ginsburg A., Carrasco-González C., Liu H. B., Rodríguez L. F., Kurtz S., 2018, in Murphy E., ed., ASP Conf. Ser. Vol. 517, Resolving the Structure and Kinematics of the Youngest HII Regions and Radio Jets from Young Stellar Objects. Astron. Soc. Pac., San Francisco, p. 309
Garay G., Brooks K. J., Mardones D., Norris R. P., 2003, ApJ, 587, 739
Garcia P. J. V., Ferreira J., Cabrit S., Binette L., 2001, A&A, 377, 589
Giacalone J., Jokipii J. R., 2007, ApJ, 663, L41
Goddi C., Surcis G., Moscadelli L., Imai H., Vlemmings W. H. T., van Langevelde H. J., Sanna A., 2017, A&A, 597, A43
Hartigan P., 1989, ApJ, 339, 987
Hartigan P., Edwards S., Pierson R., 2004, ApJ, 609, 261
Hartigan P., Frank A., Varniére P., Blackman E. G., 2007, ApJ, 661, 910
Hennebelle P., Falgarone E., 2012, A&AR, 20, 55
Henriksen R. N., Mirabel I. F., Ptuskin V. S., 1991, A&A, 248, 221
Hull C. L. H., Carrasco-González C., Williams P. K. G., Girart J. M., Robishaw T., Galván-Madrid R., Bourke T., 2018, in Murphy E., ed., ASP Conf. Ser. Vol. 517, Magnetic Fields in Forming Stars with the ngVLA. Astron. Soc. Pac., San Francisco, p. 357
Inoue T., Yamazaki R., Inutsuka S.-I., 2009, ApJ, 695, 825
Jean P., Gillard W., Marcowith A., Ferrière K., 2009, A&A, 508, 1099
Krause M., 2003, A&A, 398, 113
Krymskii G. F., 1977, Sov. Phys. - Dokl., 22, 327
Lang K. R., 1974, Astrophysical Formulae: A Compendium for the Physicist and Astrophysicist. Springer, Berlin
Lee C.-F., Hwang H.-C., Ching T.-C., Hirano N., Lai S.-P., Rao R., Ho P. T. P., 2018, Nat. Commun., 9, 4636
Li C. K., Tikhonchuk V. T., Moreno Q. E. A., 2019, Phys. Rev. Lett., 123, 055002
Liang G. Y. et al., 2018, ApJ, 868, 56
Marcowith A. et al., 2016, Rep. Prog. Phys., 79, 046901
Marcowith A., Casse F., 2010, A&A, 515, A90
Marcowith A., Dwarkadas V. V., Renaud M., Tatischeff V., Giacinti G., 2018, MNRAS, 479, 4470
Marti J., Rodriguez L. F., Reipurth B., 1993, ApJ, 416, 208
Masqué J. M., Girart J. M., Estalella R., Rodríguez L. F., Beltrán M. T., 2012, ApJ, 758, L10
Matthews J. H., Bell A. R., Blundell K. M., Araudo A. T., 2017, MNRAS, 469, 1849
Maurri L., Bacciotti F., Podio L., Eislöffel J., Ray T. P., Mundt R., Locatelli U., Coffey D., 2014, A&A, 565, A110
Moll R., 2009, A&A, 507, 1203
Nicolaï P., Stenz C., Kasperczuk A. E. A., 2008, Phys. Plasmas, 15, 082701
Norman C., Silk J., 1979, ApJ, 228, 197
Obonyo W. O., Lumsden S. L., Hoare M. G., Purser S. J. D., Kurtz S. E., Johnston K. G., 2019, MNRAS, 486, 3664
Osorio M. et al., 2017, ApJ, 840, 36
Padovani M., Hennebelle P., Marcowith A., Ferrière K., 2015, A&A, 582, L13
Padovani M., Marcowith A., Hennebelle P., Ferrière K., 2016, A&A, 590, A8
Parizot E., Marcowith A., Ballet J., Gallant Y. A., 2006, A&A, 453, 387
Park J., Caprioli D., Spitkovsky A., 2015, Phys. Rev. Lett., 114, 085003
Pelletier G., Pudritz R. E., 1992, ApJ, 394, 117
Pelletier G., Lemoine M., Marcowith A., 2006, A&A, 453, 181
Petrosian V., 2001, ApJ, 557, 560
Podio L., Lefloch B., Ceccarelli C., Codella C., Bachiller R., 2014, A&A, 565, A64
Purser S. J. D. et al., 2016, MNRAS, 460, 1039
Raga A. C., Binette L., Canto J., Calvet N., 1990, ApJ, 364, 601
Raga A. C., Canto J., Cabrit S., 1998, A&A, 332, 714
Raga A. C., Noriega-Crespo A., Velázquez P. F., 2002, ApJ, 576, L149
Reipurth B., Bally J., 2001, ARA&A, 39, 403
Reville B., Kirk J. G., Duffy P., O'Sullivan S., 2007, A&A, 475, 435
Reville B., Kirk J. G., Duffy P., 2009, ApJ, 694, 951
Reville B., Bell A. R., Gregori G., 2013, New J. Phys., 15, 015015
Rodríguez L. F., Garay G., Brooks K. J., Mardones D., 2005, ApJ, 626, 953
Rodríguez-Kamenetzky A. et al., 2017, ApJ, 851, 16
Rodríguez-Kamenetzky A., Carrasco-González C., González-Martín O., Araudo A. T., Rodríguez L. F., Vig S., Hofner P., 2019, MNRAS, 482, 4687
Schure K. M., Bell A. R., 2014, MNRAS, 437, 2802
Shu F., Najita J., Ostriker E., Wilkin F., Ruden S., Lizano S., 1994, ApJ, 429, 781
Suzuki-Vidal F., Bocchi M., Lebedev E. A., 2012, Phys. Plasmas, 19, 022708
Suzuki-Vidal F., Lebedev S. V., Ciardi A., Pickworth L. A., Rodriguez R., Gil J. M., Espinosa G., Hartigan P., 2015, ApJ, 815, 96
Teşileanu O., Mignone A., Massaglia S., Bacciotti F., 2012, ApJ, 746, 96
Tzeferacos P. et al. 2018, Nat. Commun., 9, 591
van Marle A. J., Casse F., Marcowith A., 2018, MNRAS, 473, 3394
Vink J., Laming J. M., 2003, ApJ, 584, 758
Vurm I., Metzger B. D., 2018, ApJ, 852, 62
Xu S., Lazarian A., 2017, ApJ, 850, 126
Yirak K., Schroeder E., Frank A., Cunningham A. J., 2012, ApJ, 746, 133
Zirakashvili V. N., Ptuskin V. S., 2008, ApJ, 678, 939
Zweibel E. G., Everett J. E., 2010, ApJ, 709, 1412

APPENDIX A: SYNCHROTRON EMISSION

The synchrotron emissivity per unit frequency ν emitted by a source with volume $V_{\rm e}$ located at distance d from Earth is $\epsilon_{{\rm syn},\,\nu} = 4\pi d^2 S_\nu / V_{\rm e}$, giving

$$\frac{\epsilon_{{\rm syn},\nu}}{{\rm erg\,Hz^{-1}s^{-1}cm^{-3}}} = \frac{1.2\times10^{-30}}{f_{\rm Ve}}\left(\frac{d}{\rm kpc}\right)^2\left(\frac{S_\nu}{\rm mJy}\right)\left(\frac{R}{10^{16}{\rm cm}}\right)^{-3}, \tag{A1}$$

where S_ν is the flux at frequency ν. We have defined $V_{\rm e} = f_{\rm Ve} R_{\rm j}^3$, where $V_{\rm e}$ is the volume filled in with non-thermal electrons and $f_{\rm Ve}$ is the volume-filling factor. We consider that $\epsilon_{{\rm syn},\,\nu} = 4\pi\varepsilon_\nu$, where the emission coefficient for synchrotron radiation is

$$\varepsilon_\nu = c_5 K_{\rm e} \langle \sin\Theta^{\frac{s+1}{2}}\rangle B_s^{\frac{s+1}{2}} \left(\frac{\nu}{2c_1}\right)^{\frac{1-s}{2}}, \tag{A2}$$

Θ is the electron pitch angle, $c_1 = 6.264\times10^{18}$ Hz and

$$c_5 = \frac{1.866\times10^{-23}}{(s+1)}\Gamma\left(\frac{3s-1}{12}\right)\Gamma\left(\frac{3s+19}{12}\right)\ {\rm erg\,G^{-1}\,sterad^{-1}} \tag{A3}$$

(Beck & Krause 2005; Arbutina et al. 2012). We assume an isotropic distribution for the orientation of Θ and therefore

$$\langle \sin\Theta^{\frac{s+1}{2}}\rangle = \frac{\sqrt{\pi}}{2}\frac{\Gamma\left(\frac{s+5}{4}\right)}{\Gamma\left(\frac{s+7}{4}\right)}. \tag{A4}$$

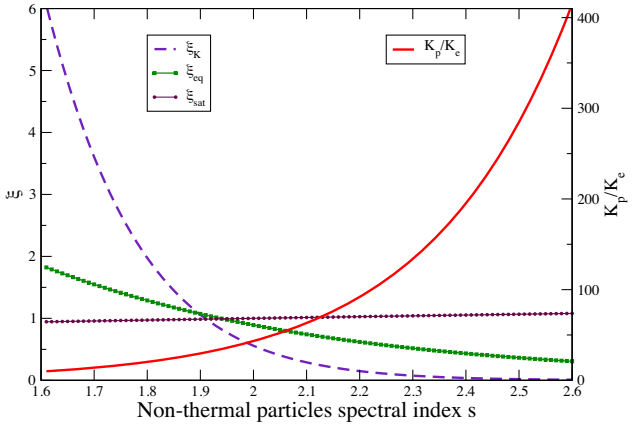

Figure A1. Functions ξ_K (equation A6), $\xi_{\rm eq}$, and $\xi_{\rm sat}$ (left y-axis) and $K_{\rm p}/K_{\rm e}$ (right y-axis) as a function of the spectral index of non-thermal particles.

By combining equations (A1)–(A4) we find that

$$\frac{K_{\rm e}}{\rm erg^{s-1}\,cm^{-3}} \approx 1.6\times10^{-9}\frac{\xi_K(s)}{f_{\rm Ve}}\left(\frac{d}{\rm kpc}\right)^2\left(\frac{S_\nu}{\rm mJy}\right)\left(\frac{R}{10^{16}\rm cm}\right)^{-3} \times\left(\frac{\nu}{\rm GHz}\right)^{\frac{s-1}{2}}\left(\frac{B_{\rm s}}{\rm mG}\right)^{-\frac{s+1}{2}}, \tag{A5}$$

where

$$\xi_K(s)\simeq 10^{-3.55(s-2)}\frac{\Gamma\left(\frac{s+5}{4}\right)\Gamma\left(\frac{3s-1}{12}\right)\Gamma\left(\frac{3s+19}{12}\right)}{\Gamma\left(\frac{s+7}{4}\right)(s+1)}. \tag{A6}$$

The function $\xi_K(s)$ is plotted in Fig. A1.

APPENDIX B: PARTICLE ENERGY DISTRIBUTION IN THE SHOCK DOWNSTREAM REGION

Non-thermal particles accelerated in a non-relativistic shock follow a power-law energy distribution

$$N_{\rm e,p}=\begin{cases} K_{\rm e,p}m_{\rm e,p}c^2{}^{\frac{(1-s)}{2}}E_{\rm e,p}^{-\frac{s+1}{2}} & E_{\rm inj}<E_{\rm e,p}<m_{\rm e,p}c^2,\\ K_{\rm e,p}E_{\rm e,p}^{-s} & m_{\rm e,p}c^2<E_{\rm e,p}<E_{\rm e,p,max},\end{cases} \tag{B1}$$

where e and p stands for electrons and protons, respectively, and $E_{\rm inj}\sim 2m_{\rm p}v_{\rm sh}^2$. We note that the condition $N_{\rm e}=N_{\rm p}$ at $E<m_{\rm e}c^2$ gives $K_{\rm p}/K_{\rm e}=(m_{\rm p}/m_{\rm e})^{(s-1)/2}$ (see Fig. A1). The spectrum is flatter in the non-relativistic regime, and therefore non-relativistic particles do not contribute significantly to the total energy density $U_{\rm e,p}$ and hence most of the non-thermal number and energy density is due to particles with $E_{\rm e,p}\gtrsim m_{\rm e,p}c^2$. In the case of negligible energy losses, the total energy density stored in non-thermal particles is

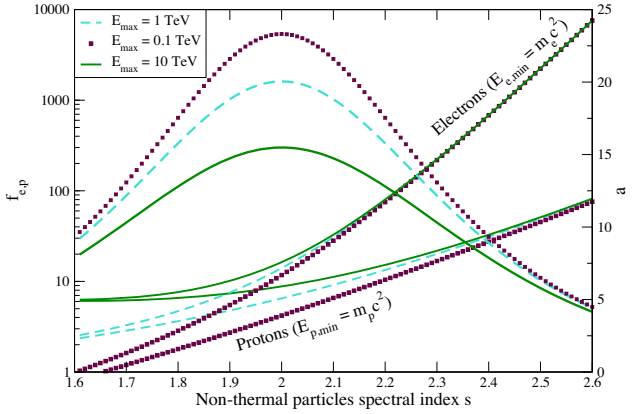

Figure B1. Functions $f_{\rm e}$ and $f_{\rm p}$ (left axis) and a (right axis) as a function of the spectral index of non-thermal particles for different values of $E_{\rm e,max}$ and $E_{\rm p,max}$.

$U_{\rm e,p,tot}=K_{\rm e,p}f_{\rm e,p}(s)$, where

$$f_{\rm e,p}\sim\begin{cases}\left(\frac{1}{2-s}\right)E_{\rm e,p,max}^{2-s} & \text{if } s<2\\ \log\left(\frac{E_{\rm e,p,max}}{m_{\rm e,p}c^2}\right) & \text{if } s=2\\ \left(\frac{1}{s-2}\right)(m_{\rm e,p}c^2)^{2-s} & \text{if } s>2.\end{cases} \tag{B2}$$

We note that the ratio $a=U_{\rm p,tot}/U_{\rm etot}$ can be written as $a=(m_{\rm p}/m_{\rm e})^{(s-1)/2}f_{\rm p}/f_{\rm e}$, and for $s>2$ it can be approximated as $a\sim(m_{\rm p}/m_{\rm e})^{(3-s)/2}$. In Fig. B1, we plot $f_{\rm p}$, $f_{\rm e}$, and a for $1.6\le s\le 2.6$ and $E_{\rm e,max}=E_{\rm p,max}=0.1$, 1, and 10 TeV.

The energy and number density of particles with a certain energy $E_{\rm e,p}$ are $n_{\rm e,p}=K_{\rm e,p}E_{\rm e,p}^{1-s}$ and $U_{\rm e,p}=K_{\rm e,p}E_{\rm e,p}^{2-s}$, respectively. We are particularly interested in protons, given that they are responsible for the CR streaming instability. The number and energy density of protons with energy $E_{\rm p}$ are

$$n_{\rm p}=\frac{U_{\rm p,tot}}{\rm f_p}E_{\rm p}^{1-s}\sim\begin{cases}\left(\frac{U_{\rm p,tot}}{E_{\rm p,max}}\right)(2-s)\left(\frac{E_{\rm p}}{E_{\rm p,max}}\right)^{1-s} & \text{if } s<2\\ \frac{U_{\rm p,tot}}{m_{\rm p}c^2\log\left(\frac{E_{\rm p,max}}{mc^2}\right)}\left(\frac{E_{\rm p}}{m_{\rm p}c^2}\right)^{-1} & \text{if } s=2\\ \left(\frac{U_{\rm p,tot}}{m_{\rm p}c^2}\right)(s-2)\left(\frac{E_{\rm p}}{m_{\rm p}c^2}\right)^{1-s} & \text{if } s>2\end{cases} \tag{B3}$$

and

$$U_{\rm p}=\frac{U_{\rm p,tot}}{f_{\rm p}}E_{\rm p}^{2-s}\sim\begin{cases}U_{\rm p,tot}(2-s)\left(\frac{E_{\rm p}}{E_{\rm p,max}}\right)^{2-s} & \text{if } s<2\\ \frac{U_{\rm p,tot}}{\log\left(\frac{E_{\rm p,max}}{m_{\rm p}c^2}\right)} & \text{if } s=2\\ U_{\rm p,tot}(s-2)\left(\frac{E_{\rm p}}{m_{\rm p}c^2}\right)^{2-s} & \text{if } s>2,\end{cases} \tag{B4}$$

respectively.

This paper has been typeset from a TEX/LATEX file prepared by the author.